Neutron dominance in excited states of ^{26}Mg and ^{10}Be probed by proton and α inelastic scattering

Yoshiko Kanada-En'yo,[1] Yuki Shikata,[1] Yohei Chiba,[2,3] and Kazuyuki Ogata[2,3,4]

[1]*Department of Physics, Kyoto University, Kyoto 606-8502, Japan*

[2]*Department of Physics, Osaka City University, Osaka 558-8585, Japan*

[3]*Research Center for Nuclear Physics (RCNP), Osaka University, Ibaraki 567-0047, Japan*

[4]*Nambu Yoichiro Institute of Theoretical and Experimental Physics (NITEP), Osaka City University, Osaka 558-8585, Japan*

(Received 10 April 2020; revised 24 May 2020; accepted 26 June 2020; published 13 July 2020)

Isospin characters of nuclear excitations in ^{26}Mg and ^{10}Be are investigated via proton (p) and alpha (α) inelastic scattering. A structure model of antisymmetrized molecular dynamics (AMD) is applied to calculate the ground and excited states of ^{26}Mg and ^{10}Be. The calculation describes the isoscalar feature of the ground-band $2^+_1(K^\pi = 0^+_1)$ excitation and predicts the neutron dominance of the side-band $2^+_2(K^\pi = 2^+)$ excitation in ^{26}Mg and ^{10}Be. The p and α inelastic scattering off ^{26}Mg and ^{10}Be is calculated by microscopic coupled-channel (MCC) calculations with a g-matrix folding approach by using the matter and transition densities of the target nuclei calculated with AMD. The calculation reasonably reproduces the observed 0^+_1, 2^+_1, and 2^+_2 cross sections of ^{26}Mg $+p$ scattering at incident energies $E_p = 24$ and 40 MeV and of ^{26}Mg $+\alpha$ scattering at $E_\alpha = 104$ and 120 MeV. For ^{10}Be $+p$ and ^{10}Be $+\alpha$ scattering, inelastic cross sections to the excited states in the $K^\pi = 0^+_1$ ground, $K^\pi = 2^+$ side, $K^\pi = 0^+_2$ cluster, and $K^\pi = 1^-$ cluster bands are investigated. The isospin characters of excitations are investigated via inelastic scattering processes by comparison of the production rates in the ^{10}Be $+p$, ^{10}Be $+\alpha$, and ^{10}C $+p$ reactions. The result predicts that the 2^+_2 state is selectively produced by the ^{10}Be $+p$ reaction because of the neutron dominance in the 2^+_2 excitation as in the case of the ^{26}Mg $+p$ scattering to the 2^+_2 state, whereas its production is significantly suppressed in the ^{10}C $+p$ reaction.

DOI: 10.1103/PhysRevC.102.014607

I. INTRODUCTION

Isospin characters of nuclear excitations in $Z \neq N$ nuclei have been attracting great interest. To discuss the difference between neutron and proton components in nuclear deformations and excitations, the neutron and proton transition matrix elements, M_n and M_p, have been extensively investigated by experimental works with mirror analysis of electric transitions and hadron inelastic scattering with α, p, and π^-/π^+ as well as electron inelastic scattering. The ratio M_n/M_p has been discussed with the isoscalar and isovector components of 2^+ excitations for various stable nuclei [1–6]. The simple relation $M_n/M_p = N/Z$ is naively expected for a uniform rigid rotor model, while $M_n/M_p = 1$ should be satisfied if only a $Z = N$ core part contributes to the excitation. In the analysis of the M_n/M_p ratio, it has been reported that M_n/M_p systematically exceeds N/Z in proton closed-shell nuclei. In particular, an extremely large value of the ratio was found in ^{18}O, which expresses remarkable neutron dominance of the 2^+_1 excitation [1–9]. In the opposite case, $M_n/M_p < N/Z$ of proton dominance was obtained in neutron closed-shell nuclei as discussed in Refs. [2,3].

For ^{26}Mg, the M_n/M_p ratio has been investigated for various excited states by means of lifetime measurements of mirror transitions [10], and π^-/π^+, p, and α [11–14] inelastic scattering. In those analyses, the strong state dependency of isospin characters has been found in the first and second 2^+ states. The ratio $M_n/M_p = 0.7$-1 was obtained for the $0^+_1 \to 2^+_1$ transition, whereas $M_n/M_p = 1.2$-4 was estimated for the $0^+_1 \to 2^+_2$ transition. The former indicates an approximately isoscalar nature of the 2^+_1 excitation, while the latter shows predominant neutron component of the 2^+_2 excitation. These facts suggest different isospin characters of the 2^+_1 and 2^+_2 states, which belong to the ground and side bands built on the prolate deformation, respectively. However, there remains significant uncertainty in the neutron component of the $0^+_1 \to 2^+_2$ transition.

The isospin characters of nuclear excitations are hot issues also in the physics of unstable nuclei. The neutron dominance in the 2^+_1 state has been suggested in neutron-rich nuclei such as ^{12}Be and ^{16}C [15–27]. The proton component can be determined from $B(E2)$ measured by γ decays. For the neutron component, such tools as mirror analysis and π^-/π^+ scattering are practically difficult for neutron-rich nuclei. Instead, p inelastic scattering experiments in the inverse kinematics have been intensively performed to probe the neutron component and supported the neutron dominance in the 2^+_1 state of ^{12}Be and ^{16}C. Very recently, Furuno *et al.* have achieved an α inelastic scattering experiment off ^{10}C in the inverse kinematics and discussed the isospin characters of the 2^+_1 excitation [28].

Our aim in this paper is to investigate isospin characters of the 2^+_1 and 2^+_2 excitations in ^{26}Mg and ^{10}Be with microscopic coupled-channel (MCC) calculations of p and α scattering. Structures of the ground and excited states of ^{10}Be have been studied with many theoretical models, and described well by the cluster structure of $2\alpha + nn$ (see Refs. [29–31] and

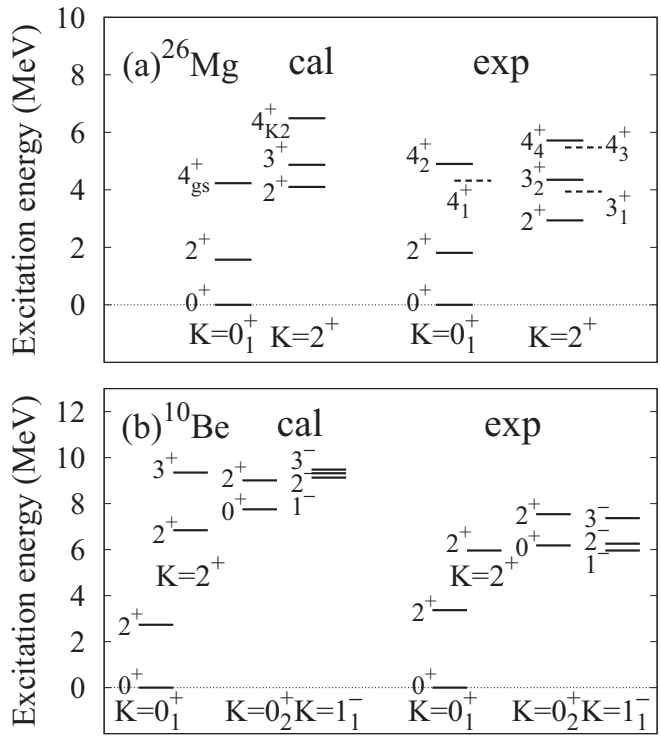

FIG. 1. Energy levels of ^{26}Mg and ^{10}Be. (a) Calculated ^{26}Mg levels of the $K^\pi = 0^+_1$ ground and $K^\pi = 2^+$ side bands compared with the experimental levels. In the experimental spectra, candidate states for 3^+ and 4^+ states of band members are shown. (b) Calculated ^{10}Be levels [46] of the $K^\pi = 0^+_1$ ground, $K^\pi = 2^+$ side, $K^\pi = 0^+_2$ cluster, and $K^\pi = 1^-$ cluster bands are shown together with the observed energy levels. The experimental data are from Refs. [52,53].

references therein). Similarly to ^{26}Mg, the 2^+_1 and 2^+_2 states of ^{10}Be are built on the prolate deformation and expected to have different isospin characters. Indeed, in Ref. [32], one of the authors (Y.K-E.) has discussed the 2^+_1 and 2^+_2 excitations of ^{10}Be and predicted the neutron dominance in the 2^+_2 excitation. We also aim to predict inelastic cross sections to cluster excitations of ^{10}Be.

In the present MCC calculations, the nucleon-nucleus potentials are microscopically derived by folding the Melbourne *g*-matrix *NN* interaction with diagonal and transition densities of target nuclei, which are obtained from microscopic structure models. The α-nucleus potentials are obtained by folding the nucleon-nucleus potentials with an α density. The MCC approach with the Melbourne *g*-matrix *NN* interaction has successfully described the observed cross sections of p and α elastic and inelastic scattering off various nuclei at 40–300 MeV of p energies and 100–400 MeV of α energies [33–39]. In our recent works [40–43], we have applied the MCC calculations by using matter and transition densities of target nuclei calculated by a structure model of antisymmetrized molecular dynamics (AMD) [30,44–46] and investigated transition properties of low-lying states of various stable and unstable nuclei via p and α inelastic scattering. One of the advantages of this approach is that one can discuss inelastic processes of different hadronic probes, p and α, in a unified treatment of a microscopic description. Another advantage is that there is no phenomenological parameter in the reaction part. Since one can obtain cross sections at given energies for given structure inputs with no ambiguity, it can test the validity of the structure inputs via p and α cross sections straightforwardly.

In this paper, we apply the MCC approach to p and α scattering off ^{26}Mg and ^{10}Be using the AMD densities of the target nuclei, and investigate isospin characters of inelastic transitions of ^{26}Mg and ^{10}Be. Particular attention is paid to transition features of the ground-band 2^+_1 state and the side-band 2^+_2 state. We also give a theoretical prediction of inelastic cross sections to cluster states of $A = 10$ nuclei of the ^{10}Be $+p$, ^{10}Be $+\alpha$, and ^{10}C $+p$ reactions.

The paper is organized as follows. The next section briefly describes the MCC approach for the reaction calculations of p and α scattering and the AMD framework for structure calculations of ^{26}Mg and ^{10}Be. Structure properties of ^{26}Mg and ^{10}Be are described in Sec. III and transition properties and p and α scattering are discussed in Sec. IV. Finally, the paper is summarized in Sec. V.

TABLE I. Calculated rms radii of proton (R_p), neutron (R_n), and matter (R_m) distributions of ^{26}Mg and ^{10}Be [46]. The experimental values of R_p of the ground state are determined from the experimental charge radii [54].

		AMD			expt.
$^AZ(J^\pi)$	band	R_p (fm)	R_n (fm)	R_m (fm)	R_p (fm)
^{26}Mg(0^+_1)	$K^\pi = 0^+_1$	3.10	3.14	3.12	2.921(2)
^{26}Mg(2^+_2)	$K^\pi = 2^+$	3.12	3.15	3.14	
^{10}Be(0^+_1)	$K^\pi = 0^+_1$	2.50	2.56	2.54	2.22(2)
^{10}Be(2^+_2)	$K^\pi = 2^+$	2.60	2.73	2.68	
^{10}Be(0^+_2)	$K^\pi = 0^+_2$	2.92	3.17	3.07	
^{10}Be(1^-_1)	$K^\pi = 1^-$	2.75	2.93	2.86	

II. METHOD

The reaction calculations of p and α scattering are performed with the MCC approach as done in Refs. [40–42]. The diagonal and coupling potentials for the nucleon-nucleus system are microscopically calculated by folding the Melbourne *g*-matrix *NN* interaction [33] with densities of the target nucleus calculated by AMD. The α-nucleus potentials are obtained in an extended nucleon-nucleus folding model [38] by folding the nucleon-nucleus potentials with an α density given by a one-range Gaussian form. In the present reaction calculations, the spin-orbit term of the potentials is not taken into account to avoid complexity as in Refs. [42,43]. It should be stressed again that there is no adjustable parameter in the reaction part. Therefore, nucleon-nucleus and α-nucleus potentials are straightforwardly obtained from given structure inputs of diagonal and transition densities. The adopted channels of the MCC calculations are explained in Sec. IV.

The structure calculation of ^{10}Be has been done by AMD with variation after parity and total angular momentum projections (VAPs) in Ref. [46]. The diagonal and transition densities obtained by AMD have been used for the MCC

TABLE II. The $E2$ transition strengths of ^{26}Mg. Theoretical values of proton [$B(E2)$] and neutron [$B_n(E2)$] components obtained by AMD, and the experimental $B(E2)$ values [52] are listed in the unit of $e^2\text{fm}^4$.

expt. transition	$B(E2)$	AMD transition	$B(E2)$	$B_n(E2)$
$2^+_1 \to 0^+_1$	61.3(2.7)	$2^+_1 \to 0^+_1$	63	39
$2^+_2 \to 0^+_1$	1.8(0.2)	$2^+_2 \to 0^+_1$	0.8	5.4
$4^+_1 \to 2^+_1$	21(1)			
$4^+_2 \to 2^+_1$	64(14)	$4^+_{gs} \to 2^+_1$	76	58
$4^+_2 \to 2^+_2$	11(3)	$4^+_{gs} \to 2^+_2$	8.8	4.9
$4^+_2 \to 3^+_2$		$4^+_{gs} \to 3^+_{K2}$	39	29
$4^+_3 \to 2^+_1$	5.0(1.8)			
$4^+_3 \to 3^+_1$	55(23)			
$4^+_4 \to 2^+_1$		$4^+_{K2} \to 2^+_1$	11.4	3.5
$4^+_4 \to 2^+_2$	7.8(2.3)	$4^+_{K2} \to 2^+_2$	22	11
$4^+_4 \to 3^+_1$	1.8(0.9)			
$4^+_4 \to 3^+_2$	14(6)	$4^+_{K2} \to 3^+_{K2}$	39	22
$3^+_2 \to 2^+_1$	0.3(0.2)	$3^+_{K2} \to 2^+_1$	1.5	9.4
$3^+_2 \to 2^+_2$	41(18)	$3^+_{K2} \to 2^+_2$	114	66

calculation of the ^{10}Be $+p$ reaction in the previous work [42]. We adopt the AMD results of ^{10}Be as structure inputs of the present MCC calculations of the ^{10}Be $+p$ and ^{10}Be $+\alpha$ reactions. For ^{26}Mg, we apply the AMD + VAP with fixed nucleon spins in the same way Ref. [43] for ^{28}Si. Below, we briefly explain the AMD framework of the present calculation of ^{26}Mg. This calculation is an extension of the previous AMD calculation of ^{26}Mg in Ref. [32]. For more details, the reader is referred to the previous works and references therein.

An AMD wave function of a mass-number A nucleus is given by a Slater determinant of single-nucleon Gaussian wave functions as

$$\Phi_{\text{AMD}}(\boldsymbol{Z}) = \frac{1}{\sqrt{A!}}\mathcal{A}\{\varphi_1, \varphi_2, \ldots, \varphi_A\}, \tag{1}$$

$$\varphi_i = \phi_{X_i}\chi_i\tau_i, \tag{2}$$

$$\phi_{X_i}(\boldsymbol{r}_j) = \left(\frac{2\nu}{\pi}\right)^{3/4} \exp[-\nu(\boldsymbol{r}_j - \boldsymbol{X}_i)^2]. \tag{3}$$

Here $\mathcal{A}$ is the antisymmetrizer, and φ_i is the ith single-particle wave function given by a product of spatial (ϕ_{X_i}), nucleon-spin (χ_i), and isospin (τ_i) wave functions. In the present calculation of ^{26}Mg, we fix nucleon spin and isospin functions as spin-up and spin-down states of protons and neutrons. Gaussian centroid parameters $\{\boldsymbol{X}_i\}$ for single-particle wave functions are treated as complex variational parameters independently for all nucleons.

In the model space of the AMD wave function, we perform energy variation after total-angular-momentum and parity projections (VAP). For each J^π state, the variation is performed with respect to the J^π-projected wave function $P^{J\pi}_{MK}\Phi_{\text{AMD}}(\boldsymbol{Z})$ to obtain the optimum parameter set of Gaussian centroids $\{\boldsymbol{X}_i\}$. Here $P^{J\pi}_{MK}$ is the total angular momentum and parity projection operator. In the energy variation, $K = 0$ is taken for the $J^\pi = 0^+$, 2^+, and 4^+ states in the $K^\pi = 0^+_1$ ground band, and $K = 2$ is chosen for the $J^\pi = 2^+$ and 3^+ states in the $K^\pi = 2^+$ side band. After the energy variation of these states, we obtain five basis wave functions. To obtain final wave functions of ^{26}Mg, mixing of the five configurations (configuration mixing) and K mixing are taken into account by diagonalizing the norm and Hamiltonian matrices.

TABLE III. Transition strengths and matrix elements of the isoscalar monopole (IS0) and dipole (IS1), and $E\lambda$ transitions. The calculated values are the isoscalar ($p + n$), proton, and neutron components of the transition strengths, the proton and neutron transition matrix elements, and the M_n/M_p ratio obtained by AMD [46]. The experimental values are $E2$ transition strengths of ^{10}Be and ^{10}C, and M_p, M_n, and M_n/M_p from Ref. [53]. The units of $B(E\lambda)$ and $B(\text{IS0}\lambda)$ are $e^2\text{fm}^{2\lambda}$ and $e^2\text{fm}^{2\lambda+4}$, respectively. The units of $M_{p,n}$ are $e\,\text{fm}^\lambda$ and $e\,\text{fm}^{\lambda+2}$ for $E\lambda$ and ISλ transitions, respectively.

			AMD			
	B_{p+n}(IS0)	B_p(IS0)	B_n(IS0)	M_p	M_n	M_n/M_p
$0^+_2 \to 0^+_1$	12.7	1.5	5.4	1.2	2.3	1.89
	$B_{p+n}(E2)$	$B(E2)$	$B_n(E2)$			
$2^+_1 \to 0^+_1$	41	11.6	8.9	7.6	6.7	0.88
$2^+_2 \to 0^+_1$	1.7	0.2	3.2	−1.0	4.0	−3.9
$2^+_3 \to 0^+_1$	1.5	0.1	0.7	0.8	1.9	2.5
$2^+_3 \to 0^+_2$	280	34	118	13.1	24.3	1.85
$0^+_2 \to 2^+_1$	6.0	0.6	2.9	0.7	1.7	2.3
	B_{p+n}(IS1)	B_p(IS1)	B_n(IS1)			
$1^-_1 \to 0^+_1$	6.0	1.0	2.1	1.7	2.5	1.46
	$B_{p+n}(E3)$	$B(E3)$	$B_n(E3)$			
$3^-_1 \to 0^+_1$	70	1.3	53	3.0	19.2	6.4
			expt.			
		$B(E2)$	$B(^{10}\text{C}; E2)$	M_p	M_n	M_n/M_p
$2^+_1 \to 0^+_1$		10.2(1.0)	12.2(1.9)	7.2(0.4)	7.8(0.6)[a]	1.08[a]
$0^+_2 \to 2^+_1$		3.2(1.2)		1.8(0.4)		

[a]The empirical values of M_n and M_n/M_p evaluated from the mirror transition assuming the mirror symmetry.

In the present calculation of ^{26}Mg, the width parameter $\nu = 0.15$ fm^{-2} is used. The effective nuclear interactions of structure calculation for ^{26}Mg are the MV1 (case 1) central force [47] supplemented by a spin-orbit term of the G3RS force [48,49]. The Bartlett, Heisenberg, and Majorana parameters of the MV1 force are $b = h = 0$ and $m = 0.62$, and the spin-orbit strengths are $u_I = -u_{II} = 2800$ MeV. The Coulomb force is also included. All these parameters of the Gaussian width and effective interactions are the same as those used in the previous studies of ^{26}Mg, ^{26}Si, and ^{28}Si of Refs. [18,32]. A difference is the variational procedure. The variation was done before the total angular momentum projection in the previous studies, but it is done after the total angular momentum projection in the present AMD + VAP calculation.

III. ENERGY LEVELS, RADII, AND $B(E2)$ OF TARGET NUCLEI

A. Structure of ^{26}Mg

The ground and excited states of ^{26}Mg obtained after the diagonalization contain some amount of the configu-

TABLE IV. The transition matrix elements (M_p and M_n in the unit of e fm$^\lambda$) and the ratios (M_n/M_p), and the scaling factors ($f_p^{\rm tr}$ and $f_n^{\rm tr}$) for the renormalization of transition densities. For use of the default MCC calculations, the scaling factors $f_p^{\rm tr}$ and $f_n^{\rm tr}$ for the proton and neutron components are determined so as to fit the experimental M_p and M_n values, respectively. Theoretical values before (theor.) and after (default MCC) the renormalization are shown together with the experimental values [52,53]. For the $E2; 2_2^+ \to 0_1^+$ transition of ^{26}Mg, two optional sets (case 1 and case 2) of $f_{p,n}^{\rm tr}$ are considered in addition to the default scaling.

	M_p	M_n	M_n/M_p	$f_p^{\rm tr}$	$f_n^{\rm tr}$
^{26}Mg($E2: 2_1^+ \to 0_1^+$)					
expt.	17.5(0.4)	17.0(1.0)[a]	0.97		
theor.	17.7	13.9	0.79	1	1
MCC (default)	17.5	17.0	0.97[a]	0.99	1.22
^{26}Mg($E2: 2_2^+ \to 0_1^+$)					
expt.	3.0(0.1)	5.7(0.6)[a]	1.90[a]		
theor.	2.0	5.2	2.65	1	1
MCC (default)	3.0	5.7	1.90	1.52	1.09
MCC (case 1)	3.0	7.9	2.65	1.52	1.52
MCC (case 2)	4.3	4.3	1.00	2.20	0.83
^{26}Mg($E4: 4_2^+ \to 0_1^+$)					
expt. (e, e')	161(21)				
theor.	119	118	0.99	1	1
MCC (default)	162	161	0.99	1.36	1.36
^{26}Mg($E4: 4_4^+ \to 0_1^+$)					
expt. (e, e')	114(20)				
theor.	123	105	0.85	1	1
MCC (default)	114	97	0.85	0.93	0.93
^{10}Be($E2: 2_1^+ \to 0_1^+$)					
expt.	7.2(0.4)	7.8(0.6)[b]	1.08[b]		
theor.	7.6	6.7	0.88	1	1
MCC (default)	7.2	7.8	1.09	0.94	1.17

[a]The M_n values of ^{26}Mg are estimated from the mirror transitions with correction 0.909 of charge effects. This correction was given for $A = 18$ in Ref. [61] and used arbitrarily for $A = 26$ nuclei as done in Ref. [10].

[b]The M_n value of ^{10}Be from the mirror transition assuming the mirror symmetry (no charge effect) for $A = 10$ nuclei.

ration and K mixing, but they are approximately classified into the $K^\pi = 0_1^+$ band built on the 0_1^+ state and those in the $K^\pi = 2^+$ band starting from the 2_2^+ state. In Fig. 1(a), the calculated energy spectra are shown in comparison with the experimental spectra of candidate states for the $K^\pi = 0_1^+$ and $K^\pi = 2^+$ band members. The experimental 0_1^+, $2_1^+(1.81)$, and $4_2^+(4.90)$ states are considered to belong the $K^\pi = 0_1^+$ band, and the $2_2^+(2.94)$, $3_2^+(4.35)$, and $4_4^+(5.72)$ states are tentatively assigned to the $K^\pi = 2^+$ band from γ-decay properties [50]. However, there are other candidates such as the $3_1^+(3.94)$, $4_1^+(4.32)$, and $4_3^+(5.48)$ states in the same energy region. We denote the theoretical states in the $K^\pi = 0_1^+$ band as $J^\pi = \{0_1^+, 2_1^+,$ and $4_{\rm gs}^+\}$ and those in the $K^\pi = 2^+$ band as $J^\pi = \{2_2^+, 3_{K2}^+,$ and $4_{K2}^+\}$, and tentatively assign the $K^\pi = 0_1^+$ band members to $\{0_1^+, 2_1^+(1.81), 4_2^+(4.90)\}$ and the $K^\pi = 2^+$ band members to $\{2_2^+(2.94), 3_2^+(4.35), 4_4^+(5.72)\}$, though uncertainty remains in assignments of 3^+ and 4^+ states.

TABLE V. The $E2; 2^+ \to 0_1^+$ and $E4; 4^+ \to 0_1^+$ transition strengths of ^{26}Mg evaluated from the (e, e'), (p, p'), and (α, α') reactions. Electric transition strengths $B_{e,e'}(E\lambda)$ obtained by the (e, e') experiments [55], α inelastic transition rates $B_{\alpha,\alpha'}$ evaluated by (α, α') at $E_\alpha = 120$ MeV [14], and p inelastic transition rates $B_{p,p'}$ by (p, p') at $E_p = 40$ MeV [13] and $E_p = 24$ MeV [12] are shown together with the theoretical values of the proton and neutron components, $B(E\lambda)$ and $B_n(E\lambda)$, of the strengths. The units are e^2fm^4 for $\lambda = 2$ transitions and $10^2 e^2$fm^8 for $\lambda = 4$ transitions.

	expt.				AMD	
$J^\pi(E_x)$	$B_{e,e'}(E\lambda)$ Ref. [55]	$B_{\alpha,\alpha'}$ Ref. [14]	$B_{p,p'}$ Ref. [13]	$B_{p,p'}$ Ref. [12]	$B(E\lambda)$	$B_n(E\lambda)$
$2_1^+(1.81)$	53.2(3.2)	55	46(1)	37(2)	63	39
$2_2^+(2.94)$	1.3(0.3)	7.8	6.6(0.2)	5.6(0.6)	0.8	5.4
$4_1^+(4.32)$		9.7	11.0(0.8)	4.5(0.5)		
$4_2^+(4.90)$	29(8)	11.5	21(1)	10.6(0.9)	15.7	15.5
$4_3^+(5.48)$	3.8	11.5	7.7(0.6)	4.4(0.6)		
$4_4^+(5.72)$	14(6)	5.2	4(0.2)		16.8	12.2

The root-mean-square (rms) radii of proton (R_p), neutron (R_n), and matter (R_m) distributions of the band-head states of ^{26}Mg are shown in Table I. The $E\lambda$ transition strength $B(E\lambda)$ of the transition $J_i^\pi \to J_f^\pi$ is given by the proton component of the matrix element M_p as

$$B\left(E\lambda; J_i^\pi \to J_f^\pi\right) \equiv \frac{1}{2J_i+1}|M_p|^2, \tag{4}$$

and its counter part [the neutron component $B_n(E\lambda)$] is given by the neutron matrix element M_n as

$$B_n\left(E\lambda; J_i^\pi \to J_f^\pi\right) \equiv \frac{1}{2J_i+1}|M_n|^2. \tag{5}$$

The matrix elements M_p and M_n are given with the proton and neutron λ-pole operators O_p^λ and O_n^λ, respectively, as

$$M_{p,n} \equiv \left\langle J_f^\pi \middle|\middle| O_{p,n}^\lambda \middle|\middle| J_i^\pi \right\rangle. \tag{6}$$

Assuming the mirror symmetry, the neutron matrix element $M_n(T_z)$ in a nucleus with the z component T_z of the isospin can be determined by measuring the electric transition in the mirror nucleus with $T_z' = -T_z$ using the relation of $M_n(T_z) = M_p(T_z' = -T_z)$. The ratio (M_n/M_p) is predicted to be $(M_n/M_p) = (N/Z)$ by a macroscopic collective model, whereas it can be $(M_n/M_p) = 1$ for isoscalar excitations with equal contributions from neutron and proton parts [2,13].

In Table II, the theoretical values of $B(E2)$ and $B_n(E2)$ obtained by AMD, and the observed $E2$ transition strengths are listed. In each group of $\{0_1^+, 2_1^+(1.81), 4_2^+(4.90)\}$ and $\{2_2^+(2.94), 3_2^+(4.35), 4_4^+(5.72)\}$, sequences of strong γ transitions have been observed and support the assignment of the $K^\pi = 0_1^+$ and $K^\pi = 2^+$ bands. However, possible state mixing between the $4_1^+(4.32)$ and $4_2^+(4.90)$ states in the $K^\pi = 0_1^+$ band is likely because of fragmentation of $E2$ transitions to the $2_1^+(1.81)$ state. Moreover, an alternative assignment of

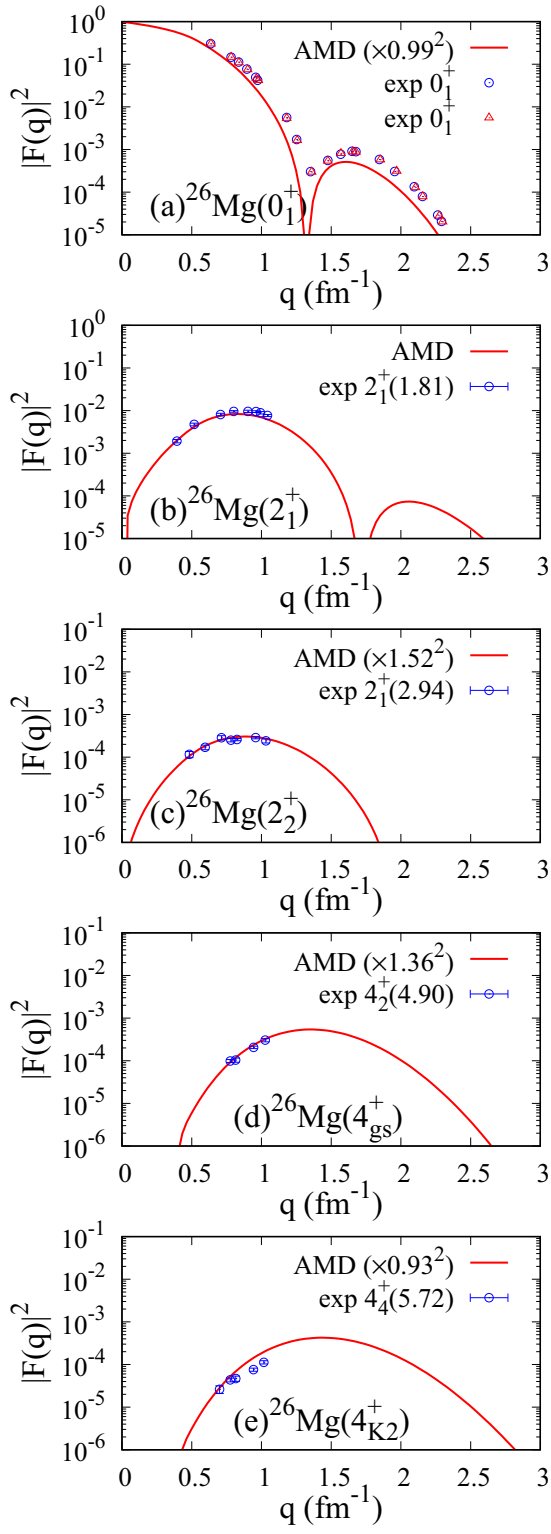

FIG. 2. Charge form factors of ^{26}Mg. The inelastic form factors $F(q)$ obtained by AMD are renormalized by $f_p^{\rm tr}$ given in Table IV. The results of the 0_1^+, 2_1^+, 2_2^+, 4_{gs}^+, and 4_{K2}^+ states are compared with the experimental data for the 0_1^+ state from Ref. [56] and those for the 2_1^+(1.81 MeV), 2_2^+(2.94 MeV), 4_2^+(4.90 MeV), and 4_4^+(5.72 MeV) states from Ref. [55].

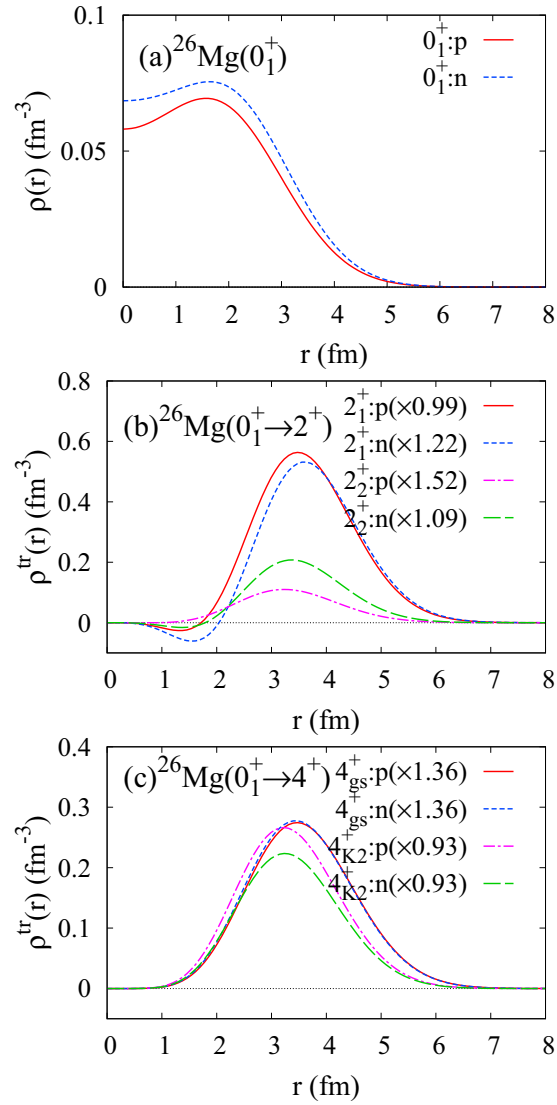

FIG. 3. Proton and neutron diagonal and transition densities of ^{26}Mg. (a) The diagonal densities of the 0_1^+ state. (b) The renormalized transition densities from the 0_1^+ state to the 2_1^+ and 2_2^+ states. (c) The renormalized transition densities from the 0_1^+ state to the 4_{gs}^+ and 4_{K2}^+ states.

the $K^\pi = 2^+$ band composed of the 2_2^+(2.94), 3_1^+(3.94), and 4_3^+(5.48) states has been suggested [51]. These experimental facts suggest that collective natures of 3^+ and 4^+ states in these bands may not be as striking as the rigid rotor picture.

In the calculated result, the in-band transition strengths $B(E2; 2_1^+ \to 0_1^+)$ and $B(E2; 4_{gs}^+ \to 2_1^+)$ of the $K^\pi = 0_1^+$ band are remarkably large and in good agreement with the experimental data for the 0_1^+, 2_1^+(1.81), and 4_2^+(4.90) states. For the $K^\pi = 2^+$ band, the calculated $B(E2)$ values of the in-band transitions, $4_{K2}^+ \to 2_2^+$, $4_{K2}^+ \to 3_{K2}^+$, and $3_{K2}^+ \to 2_2^+$, are a few times larger than the experimental $B(E2)$ of the $4_4^+ \to 2_2^+$, $4_4^+ \to 3_2^+$, and $3_2^+ \to 2_2^+$ transitions, respectively, but relative ratios between three transitions are well reproduced by the calculation. It may indicate that the observed

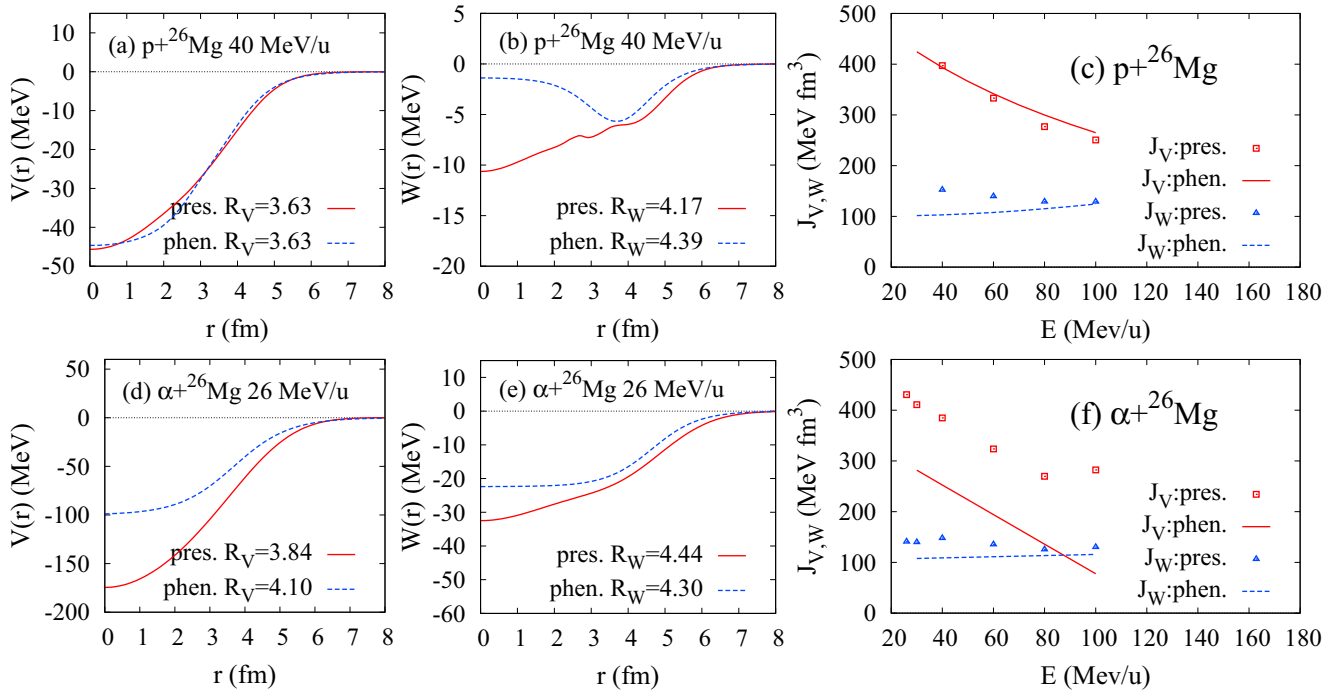

FIG. 4. Radial dependences and volume integrals of the real [$V(r)$] and imaginary [$W(r)$] parts of the present microscopic potentials (pres.) for $p + {}^{26}$Mg and $\alpha + {}^{26}$Mg elastic scattering compared with phenomenological (phen.) potentials of global optical potentials for p-nucleus [57,58] and α-nucleus [59] elastic scattering. (a), (b) $p + {}^{26}$Mg potentials at $E_p = 40$ MeV and (d), (e) $\alpha + {}^{26}$Mg potentials at $E_\alpha = 104$ MeV. In each panel, rms radii (R_V and R_W) of the potentials are shown in the unit of fm. (c), (f) Energy dependences of the volume integrals per interacting nucleon pair defined as $J_V \equiv -\int V(r)d\boldsymbol{r}/(A_pA_t)$ and $J_W \equiv -\int W(r)d\boldsymbol{r}/(A_pA_t)$ (A_p and A_t are the mass numbers of projectile and target nuclei).

$2_2^+(2.94)$, $3_2^+(4.35)$, and $4_4^+(5.72)$ states possess the $K^\pi = 2^+$ band nature but the collectivity is somewhat quenched. It should be noted that the calculation shows significant inter-band transitions between the $K^\pi = 0_1^+$ and $K^\pi = 2^+$ bands such as $4_{\rm gs}^+ \to 2_2^+$, which is consistent with the experimental $B(E2; 4_2^+ \to 2_2^+)$.

Let us discuss the neutron component [$B_n(E2)$] of the transition strengths. As seen in comparison of $B_n(E2)$ and $B(E2)$, the neutron component is comparable to or even smaller than the proton component in most cases. Exceptions are the $2_2^+ \to 0_1^+$ and $3_{K2}^+ \to 2_1^+$ transitions, which show the neutron dominance indicating the predominant neutron excitation from the $K^\pi = 0_1^+$ band to the $K^\pi = 2^+$ band. This means the different isospin characters between two 2^+ states, the 2_1^+ state in the $K^\pi = 0_1^+$ ground band and the 2_2^+ state in the $K^\pi = 2^+$ side band. The former shows the approximately isoscalar feature and the latter has the neutron dominance character.

B. Structure of ^{10}Be

In the AMD calculation of ^{10}Be, the $2\alpha + nn$ cluster structures are obtained in the ground and excited states as discussed in Ref. [46]. The $K^\pi = 0_1^+$ ground and $K^\pi = 2^+$ side bands are constructed. In addition, the $K^\pi = 0_2^+$ and $K^\pi = 1_1^-$ cluster bands are obtained. The energy spectra of ^{10}Be are shown in Fig. 1(b). The calculated energy levels are in reasonable agreement with the experimental spectra. The calculated rms proton, neutron, and matter radii of the band-head states are given in Table I. The present AMD calculation overestimates the experimental value of the rms proton radius of the ground state by approximately 10%, suggesting that the calculation may contain model ambiguity in the rms neutron radius. The overestimation of the radii in the ground state of ^{10}Be may somewhat shift peak and dip positions of elastic cross sections to forward angles but gives minor effects to inelastic cross sections. The $0_2^+(K^\pi = 0_2^+)$ and $1_1^-(K^\pi = 1^-)$ states of the cluster bands have relatively larger radii compared to the $0_1^+(K^\pi = 0_1^+)$ and $2^+(K^\pi = 2^+)$ states because of the developed cluster structure.

The calculated result of the transition strengths and matrix elements of the monopole (IS0), dipole (IS1), $E2$, and $E3$ transitions are summarized in Table III. The M_n/M_p ratio and the isoscalar component $B_{p+n} \equiv |M_p + M_n|^2/(2J_i + 1)$ of the transition strength are also given in the table. For experimental data, the $E2$ transition strengths and matrix elements observed for ^{10}Be and those for the mirror nucleus ^{10}C are listed. The experimental M_n value of ^{10}Be is evaluated from the mirror transition assuming the mirror symmetry (no charge effect for $A = 10$ nuclei). One of the striking features is that, in many transitions of ^{10}Be, the neutron component is dominant compared to the proton component because of contributions of valence neutrons around the 2α cluster. An exception is the $2_1^+ \to 0_1^+$ transition in the $K^\pi = 0_1^+$ ground band having the isoscalar nature of nearly equal proton and neutron components, which are generated by the 2α core rotation.

As a result, isospin characters of the ground-band 2_1^+ state and the side-band 2_2^+ state are quite different from each other.

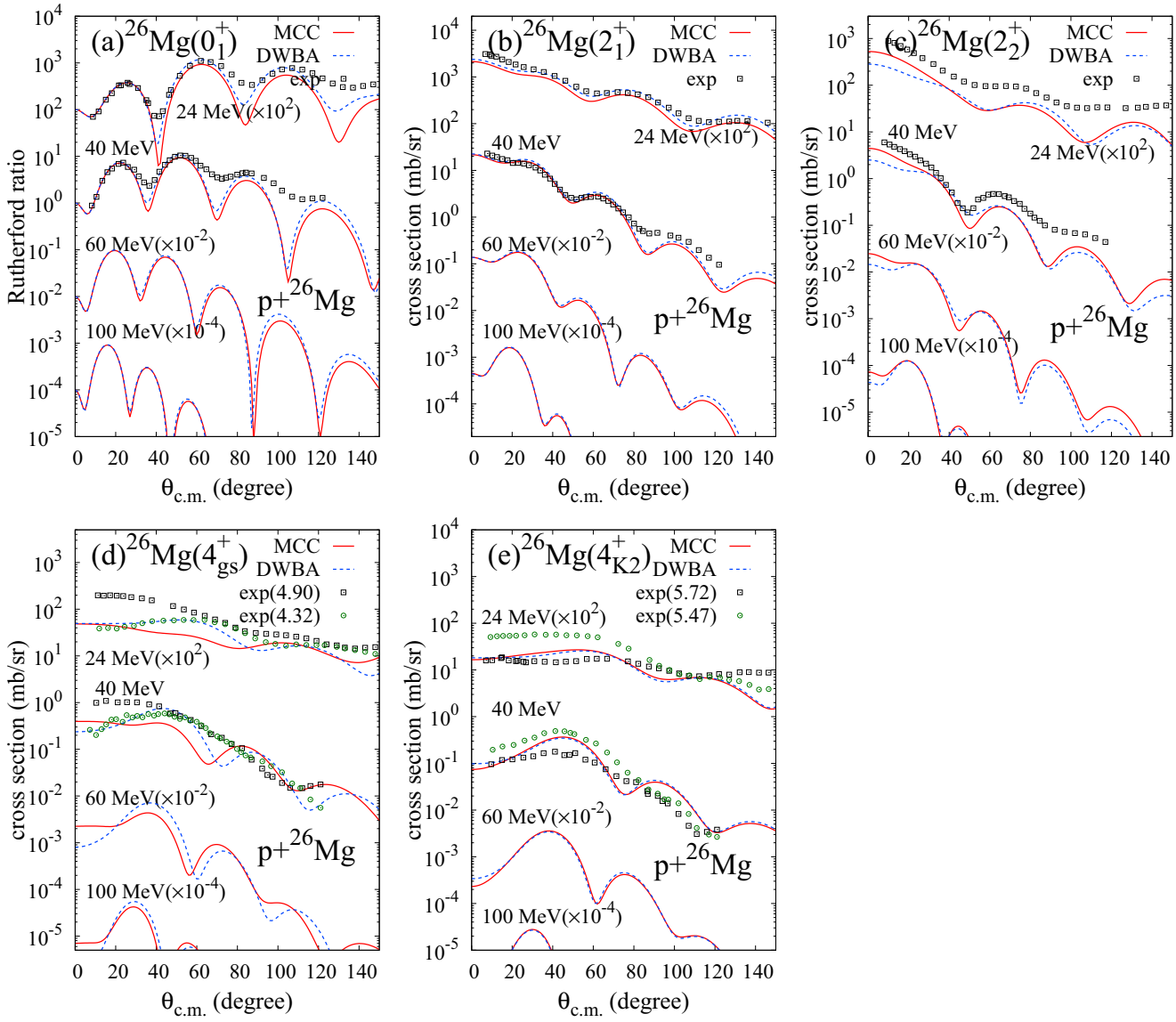

FIG. 5. Cross sections of p elastic and inelastic scattering off ^{26}Mg at $E_p = 24$, 40, 60, and 100 MeV. The results obtained by the MCC and DWBA calculations are shown by red solid and blue dashed lines, respectively. Experimental data are cross sections at $E_p = 24$ MeV [12] and 40 MeV [13] from the EXFOR database [60]. (a), (b), and (c) show the calculated and experimental cross sections of the 0^+_1, 2^+_1, and 2^+_2 states, respectively. (d) shows the calculated 4^+_{gs} cross sections together with the data observed for the 4^+_2(4.90 MeV) and 4^+_1(4.32 MeV) states. (e) shows the calculated 4^+_{K2} cross sections compared with the data observed for the 4^+_4(5.47 MeV) and 4^+_3(5.72 MeV) states.

The former has the isoscalar feature and the latter shows the neutron dominance character. This is similar to the case of ^{26}Mg and can be a general feature of $N = Z + 2$ system having a $N = Z$ core with prolate deformation. The ground-band 2^+ state is constructed by the $K = 0$ rotation of the core part with the isoscalar prolate deformation, whereas the side-band 2^+ state is described by the $K = 2$ rotation of valence neutrons around the prolate core.

IV. p AND α SCATTERING

In order to reduce model ambiguity of structure inputs, we perform fine tuning of the theoretical transition densities $\rho^{\rm tr}(r)$ by multiplying overall factors as $\rho^{\rm tr}(r) \to f^{\rm tr}\rho^{\rm tr}(r)$ to fit the observed $B(E\lambda)$ data, and utilize the renormalized transition densities $f^{\rm tr}\rho^{\rm tr}(r)$ for the MCC calculations. For each system of ^{26}Mg and ^{10}Be, we first describe the scaling factors $f^{\rm tr}$ and show the renormalized transition densities and form factors. Then, we investigate p and α scattering cross sections with the MCC calculations using the renormalized AMD densities to clarify to transition properties of excited states, in particular, their isospin characters.

A. Transition properties of ^{26}Mg

The transition matrix elements (M_p and M_n) and the scaling factors ($f^{\rm tr}_p$ and $f^{\rm tr}_p$) for the renormalization of transition densities are listed in Table IV. Theoretical values before and after

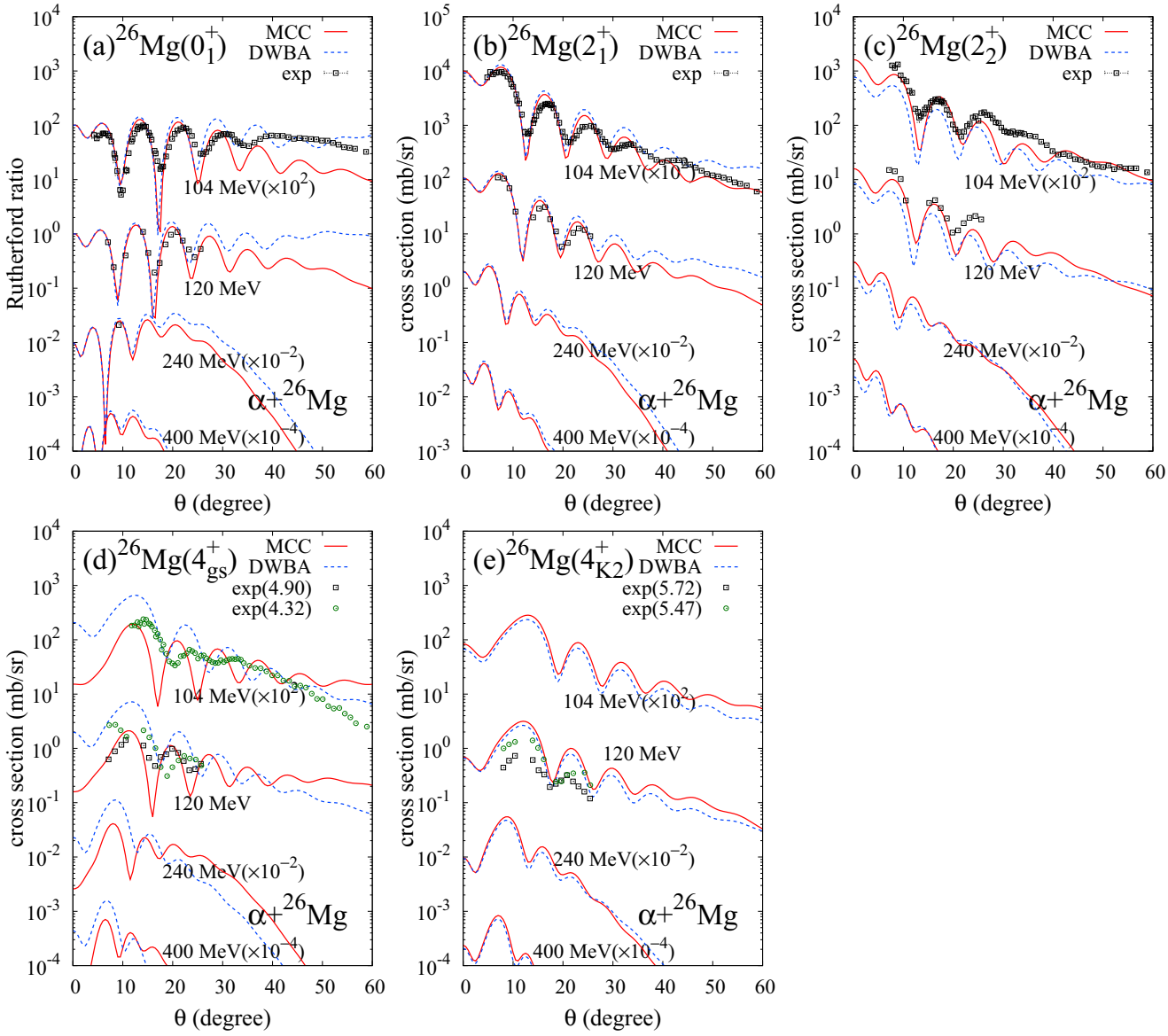

FIG. 6. Same as Fig. 5 but for α scattering at $E_\alpha = 104$, 120, 240, and 400 MeV. Experimental data at $E_\alpha = 104$ MeV [62] from the EXFOR database [60] and $E_\alpha = 120$ MeV [14] are shown.

the renormalization are shown together with the experimental M_p and M_n values used for fitting.

For renormalization of the $2^+_1 \to 0^+_1$ and $2^+_2 \to 0^+_1$ transitions, we determine the scaling factor $f_p^{\rm tr}$ of the proton transition density to fit the experimental M_p values measured by γ decays, and $f_n^{\rm tr}$ of the neutron transition density by fitting the experimental M_n values, which are evaluated from the mirror transitions with a correction factor 0.909 of charge effects [61] in the same way as Ref. [10]. In order to see the sensitivity of the cross sections to the isospin character of the $K^\pi = 2^+$ side band, we also consider two optional sets (case 1 and case 2) of $(f_p^{\rm tr}, f_n^{\rm tr})$ for the $2^+_2 \to 0^+_1$ transition, which are discussed in detail later in Sec. IV B.

For $4^+ \to 0^+_1$ transitions, $B(E4)$ has not been measured γ rays but the transition strengths have been evaluated by inelastic scattering experiments. In Table V, we list the transition strengths (or rates) of the $2^+ \to 0^+_1$ and $4^+ \to 0^+_1$ transitions: electric transition strengths $B(E\lambda)$ obtained with (e, e') data [55], α inelastic transition rates $B_{\alpha,\alpha'}$ evaluated from the (α, α') study [14], and p inelastic transition rates $B_{p,p'}$ from the (p, p') reaction [12,13]. Note that hadron scattering probes not only the proton but also the neutron components of transitions rates. In the present calculation, we adopt the $B(E4)$ values of the $4^+_2(4.90)$ and $4^+_4(5.72)$ states obtained from the (e, e') experiments to determine $f_p^{\rm tr}$ for the theoretical $4^+_{\rm gs}$ and 4^+_{K2} states, respectively. For $f_n^{\rm tr}$ of the neutron transition density, we use the same values as $f_p^{\rm tr}$.

Figure 2 shows the calculated elastic and inelastic form factors of ^{26}Mg in comparison with the experimental data. The data are well reproduced by the renormalized form factors of AMD. In Fig. 3, we show the diagonal densities and the renormalized transition densities. In the ground-band

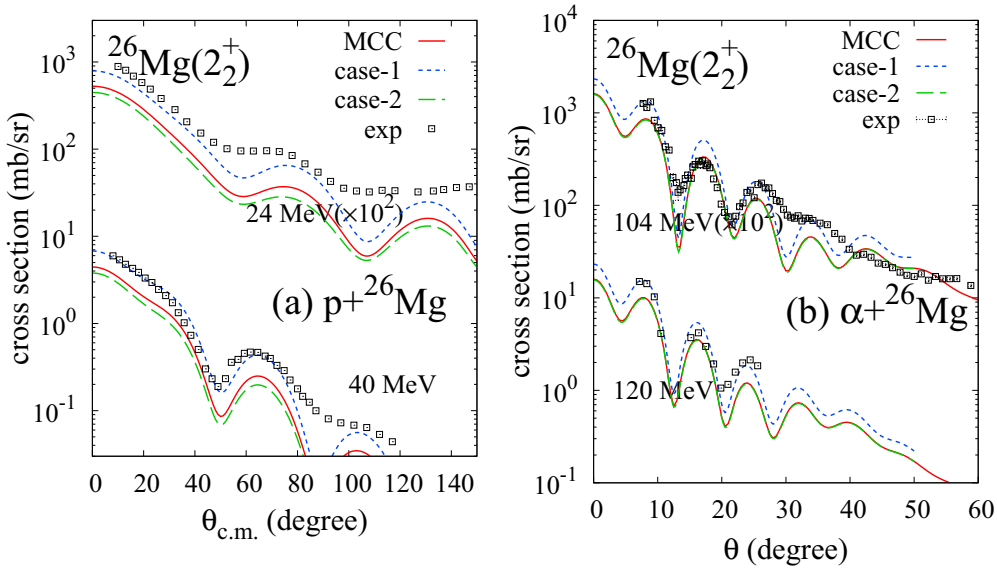

FIG. 7. 2^+_2 cross sections of the ^{26}Mg $+p$ and ^{26}Mg $+\alpha$ reactions calculated by MCC using the renormalized transition densities with the default, case 1, and case 2 scaling. (a) (p, p') cross sections at $E_p = 24$ and 40 MeV and (b) (α, α') cross sections at $E_\alpha = 104$ and 120 MeV. The experimental data of (p, p') are from Refs. [12,13,60], those of (α, α') are from Refs. [14,60,62].

transitions, $0^+_1 \to 2^+_1$ and $0^+_1 \to 4^+_{gs}$, the proton and neutron transition densities are almost the same as each other showing the isoscalar nature of those excitations in the $K^\pi = 0^+_1$ ground band. In the $0^+_1 \to 2^+_2$ excitation to the $K^\pi = 2^+$ side band, the neutron transition density is about twice larger than the proton one showing the neutron dominance, while the transition densities of $0^+_1 \to 4^+_{K2}$ show the isoscalar nature. In radial behavior of the transition densities to the 2^+_1 and 2^+_2 states, one can see that the peak position slightly shifts to the inner region in the $0^+_1 \to 2^+_2$ transition compared to the $0^+_1 \to 2^+_1$ transition.

B. ^{26}Mg $+p$ and ^{26}Mg $+\alpha$ reactions

Using the AMD densities of ^{26}Mg, we perform the MCC calculations of p scattering at $E_p = 24$, 40, 60, and 100 MeV and α scattering at $E_\alpha = 104$, 120, and 400 MeV. For coupled channels, we take into account the 0^+_1, 2^+_1, 2^+_2, 4^+_{gs}, and 4^+_{K2} states and $\lambda = 2$ and 4 transitions between them. To see coupled channel (CC) effects, we also calculate one-step cross sections with distorted wave Born approximation (DWBA). The experimental excitation energies of the 0^+_1, 2^+_1, 2^+_2, 4^+_2, and 4^+_4 states are used in the reaction calculations. For the transitions of $2^+_1 \to 0^+_1$, $4^+_{gs} \to 0^+_1$, $2^+_2 \to 0^+_1$, and $4^+_{K2} \to 0^+_1$, the renormalized transition densities are used as explained previously. For other transitions, we use theoretical transition densities without renormalization.

In Fig. 4, we show radial dependences and volume integrals of the present microscopic potentials for $p +$ ^{26}Mg and $\alpha +$ ^{26}Mg scattering compared with phenomenological optical potentials for p elastic scattering [57,58] and for α elastic scattering [59]. For both $p +$ ^{26}Mg and $\alpha +$ ^{26}Mg scattering, the present potentials, which are microscopically obtained by the g-matrix folding approach, show similar behaviors at the surface region to those of the phenomenological potentials. In the internal region, some differences between the microscopic and phenomenological potentials can be seen in the imaginary part of the $p +$ ^{26}Mg potential and the real and imaginary parts of the $\alpha +$ ^{26}Mg potential, but these differences give minor

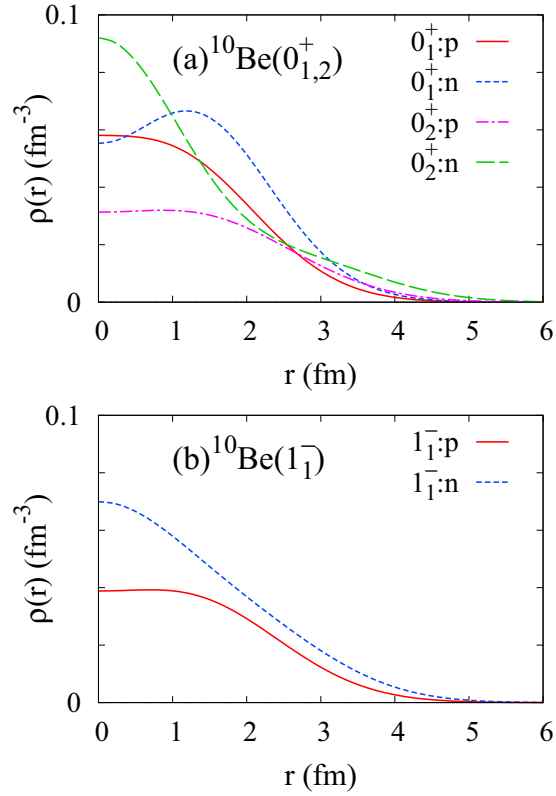

FIG. 8. Diagonal densities of ^{10}Be. The proton and neutron densities of the (a) $0^+_{1,2}$ and (b) 1^-_1 states.

contributions to elastic cross sections except for backward angles. A similar trend in the microscopic and phenomenological potentials of p scattering was shown for $p+^{40}$Ca elastic scattering in Ref. [36].

The MCC and DWBA results of the ^{26}Mg $+p$ reaction are shown in Fig. 5 together with the experimental cross sections at $E_p = 24$ and 40 MeV, and those of the ^{26}Mg $+\alpha$ reaction are shown in Fig. 6 with the experimental cross sections at $E_\alpha =$ 104 and 120 MeV. As shown in Fig. 5(a), the MCC calculation reproduces well the p elastic cross sections at $E_p = 24$ and 40 MeV. It should be commented that spin-orbit interaction, which is omitted in the present reaction calculation, may smear the deep dip structure of the calculated cross sections. The calculation also describes the experimental data of α elastic scattering at $E_\alpha = 104$ and 120 MeV [Fig. 6(a)] except for backward angles $\theta > 40^\circ$.

For the ground-band 2_1^+ state, the MCC calculation successfully reproduces the amplitudes and also the diffraction patterns of the (p, p') and (α, α') cross sections. For the inelastic scattering to the side-band 2_2^+ state, the calculation reasonably describes the (α, α') data including $E_\alpha = 104$ MeV scattering data at backward angles. However, it somewhat underestimates the (p, p') data. Comparing the DWBA and MCC results, one can see that CC effects are minor in the 2_1^+ and 2_2^+ cross sections of p scattering and 2_1^+ cross sections of α scattering but give a significant contribution to the 2_2^+ cross sections of low-energy α scattering.

For the $4^+_{\rm gs}$ and 4^+_{K2} states, agreements with the experimental (p, p') cross sections are not satisfactory enough to discuss whether the present assignment of 4^+ states is reasonable [Fig. 5(d) and Fig. 5(e)]. For the (α, α') processes, the experimental cross sections observed for the 4_2^+(4.90 MeV) state are reproduced well by the MCC result, which shows large suppression by the CC effect because of the $E2$ coupling with the 2_1^+ state in the same band [Fig. 6(d)]. For the 4^+_{K2} cross sections, the MCC calculation obtains almost no suppression by the CC effect and significantly overestimates the (α, α') data for the 4_4^+(5.72 MeV) states. We can state that p and α inelastic processes to low-lying 4^+ states are not as simple as a theoretical description with the $4^+_{\rm gs}$ and 4^+_{K2} states. Instead, they may be affected by significant state mixing and channel coupling, which are beyond the present AMD calculation. This indication is consistent with the γ decay properties.

Let us discuss isospin properties of the 2_1^+ and 2_2^+ states with further detailed analysis of the inelastic cross sections. As shown previously, the MCC calculation gives good reproduction of the 2_1^+ cross sections in describing the peak and dip structures of the (p, p') data at $E_p = 40$ MeV and (α, α') data at $E_\alpha = 120$ MeV [Fig. 5(b) and Fig. 6(b)]. For the 2_2^+ state, it describes the diffraction patterns of the (p, p') data but somewhat underestimates absolute amplitudes of the cross sections.

In order to discuss possible uncertainty in the neutron strength (or the M_n/M_p ratio) of the $0_1^+ \to 2_2^+$ transition, we consider here optional choices of the renormalization of the transition densities by changing the scaling factors $(f_p^{\rm tr}, f_n^{\rm tr})$ for this transition from the default values $(f_p^{\rm tr}, f_n^{\rm tr}) =$ (1.52, 1.09). The values of $(f_p^{\rm tr}, f_n^{\rm tr})$, M_p, M_n, and M_n/M_p for these two choices are listed in Table IV. In the case 1, we choose the same scaling for the proton and neutron parts as $(f_p^{\rm tr}, f_n^{\rm tr}) = (1.52, 1.52)$. In this case, the neutron transition

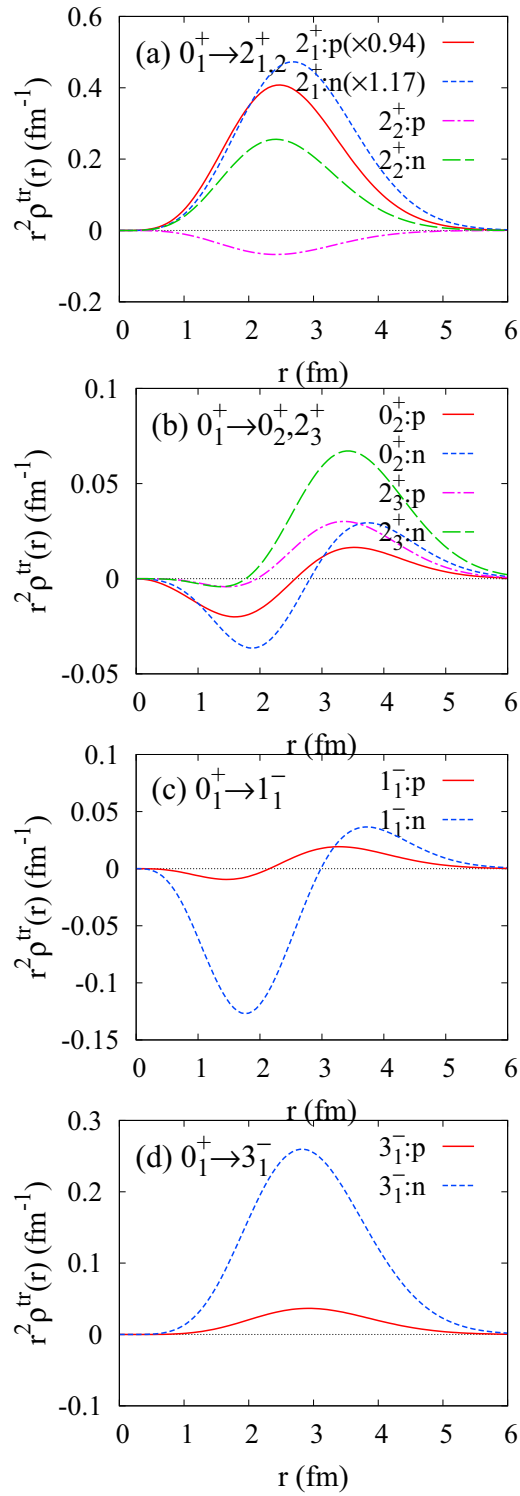

FIG. 9. Transition densities of ^{10}Be. The proton and neutron transition densities from the 0_1^+ state to the (a) $2^+_{1,2}$, (b) 0_2^+, 2_3^+, (c) 1_1^-, and (d) 3_1^- states. The $0_1^+ \to 2_1^+$ transition densities are renormalized ones.

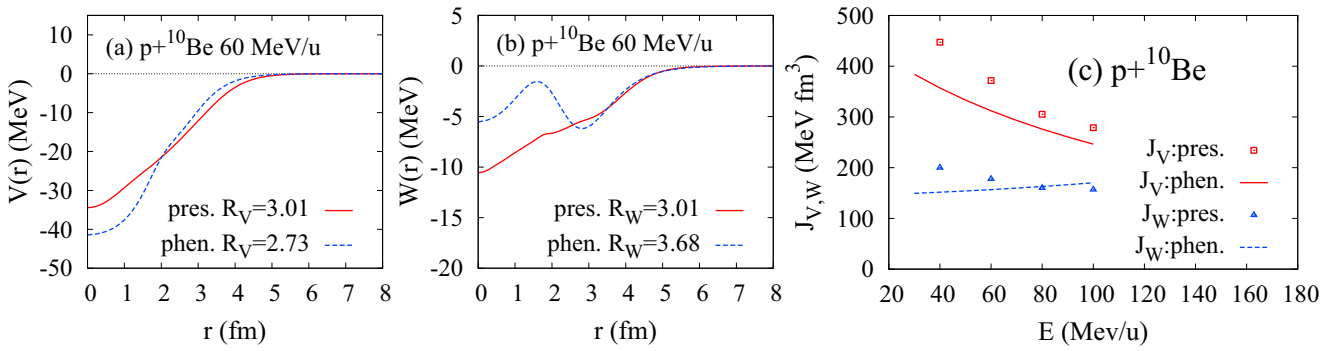

FIG. 10. Radial dependences and volume integrals of the real [$V(r)$] and imaginary [$W(r)$] parts of the present (pres.) microscopic potential for $p + {}^{10}$Be elastic scattering compared with a phenomenological potential of global optical potential [57,58]. (a), (b) $p + {}^{10}$Be potentials at $E = 60$ MeV/u. (c) Energy dependence of volume integrals $J_{V,W}$ of the potentials. In (a) and (b), rms radii (R_V and R_W) of the potentials are shown in the unit of fm.

density is enhanced by 40% from the default MCC calculation (the neutron transition strength is enhanced by a factor of two). The case 2 choice is $(f_p^{\rm tr}, f_n^{\rm tr}) = (2.20, 0.83)$, which corresponds to an assumption of the isoscalar transition $M_p = M_n$ keeping the isoscalar component $M_p + M_n$ unchanged. The value $M_n = 7.9\ e\ {\rm fm}^2$ for the case 1 becomes slightly over the upper limit of the experimental evaluation $M_n = 5.7(0.6)$ and $6.2(0.7)\ e\ {\rm fm}^2$ with and without the charge correction factor in the mirror analysis. (The value $M_n = 4.3\ e\ {\rm fm}^2$ for the case 2 goes slightly under the lower limit.) We keep other transitions to be the same as the default calculation in both cases.

In Fig. 7, we show the 2_2^+ cross sections obtained by MCC with the case 1 and case 2 choices. In the case 1 calculation, one can see that the 40% increase of the neutron transition density significantly enhances the (p, p') cross sections and slightly raises the (α, α') cross sections. As a result, the calculation well reproduces the (p, p') cross sections, in particular, at $E_p = 40$ MeV and also obtains a better result for the (α, α') cross sections. In the case 2 calculation (isoscalar assumption), the result for (p, p') cross sections becomes somewhat worse, and that for (α, α') cross sections is unchanged. This result indicates that the (p, p') process sensitively probes the dominant neutron component of the $0_1^+ \to 2_2^+$ transition and the (α, α') process can probe the isoscalar component as expected. In the present analysis, the case 1 calculation is favored to describe the 2_2^+ cross sections in both the (p, p') and (α, α') processes. This analysis supports the case 1 prediction for the $0_1^+ \to 2_2^+$ transition of the neutron transition matrix $M_n \approx 8\ {\rm fm}^2$ (the squared ratio $|M_n/M_p|^2 \approx 7$).

C. Transition properties of ^{10}Be

For ^{10}Be, experimental information of $B(E\lambda)$ is limited. For the transition from the 0_1^+ state, the available data are the observed values of $B(E2; 2_1^+ \to 0_1^+)$ and its mirror transition, with which we adjust the scaling factors of the renormalization. The transition matrix elements (M_p and M_n) and the scaling factors ($f_p^{\rm tr}$ and $f_p^{\rm tr}$) of $2_1^+ \to 0_1^+$ in ^{10}Be are given in Table IV. Theoretical values before and after the renormalization are shown together with the experimental values used for fitting. For other transitions, theoretical transition densities without the renormalization are used for the MCC calculation.

Figure 8 shows calculated diagonal densities of ^{10}Be. Compared to the ground state, the $0_2^+ (K^\pi = 0_2^+)$ and $1_1^- (K^\pi = 1^-)$ states show longer tails of the proton and neutron diagonal densities because of the developed cluster structures.

The transition densities of ^{10}Be are shown in Fig. 9. Let us compare 2^+ transitions from the 0_1^+ state to the $2_1^+ (K^\pi = 0_1^+)$, $2_2^+ (K^\pi = 2^+)$, and $2_3^+ (K^\pi = 0_2^+)$ states. In the ground-band transition, $0_1^+ \to 2_1^+$, the neutron transition density is similar to the proton one because this transition is the isoscalar excitation constructed by the $K = 0$ rotation of the 2α core part. In other transitions, the amplitude of the neutron transition density is more than twice larger than that of the proton one showing the neutron dominance in the 2_2^+ and 2_3^+ excitations. Absolute amplitude of the neutron transition density is strongest in the ground-band $0_1^+ \to 2_1^+$ transition, smaller in $0_1^+ \to 2_2^+$, and further smaller in $0_1^+ \to 2_3^+$. One of the striking features is that, in the side-band transition, $0_1^+ \to 2_2^+$, the proton component is opposite (negative sign) to the neutron one and gives cancellation effect to the isoscalar component, while the proton and neutron components are coherent in the 2_1^+ and 2_3^+ excitations. In the radial behavior of the neutron transition density, one can see that the $0_1^+ \to 2_2^+$ transition has a peak amplitude slightly shifted inward compared with $0_1^+ \to 2_1^+$ but the difference is not so remarkable. On the other hand, the $0_1^+ \to 2_3^+$ transition has amplitude shifted to the outer region.

In other inelastic transitions to the 0_2^+, 1_1^-, and 3_1^- states, the neutron transition density is dominant while the proton transition density is relatively weak indicating the neutron dominance. It should be commented that the $0_1^+ \to 0_2^+$ and $0_1^+ \to 1_1^-$ transitions show nodal structures as expected from the usual behavior of monopole and dipole transitions.

D. ^{10}Be $+p$ and ^{10}Be $+\alpha$ reactions

Using the AMD densities of ^{10}Be, we perform the MCC calculations of the ^{10}Be $+p$ and ^{10}Be $+\alpha$ reactions. For the coupled channels, we adopt the $0_{1,2}^+$, $2_{1,2,3}^+$, 1_1^-, and 3_1^- states with $\lambda = 0$, 1, 2, and 3 transitions between them. The

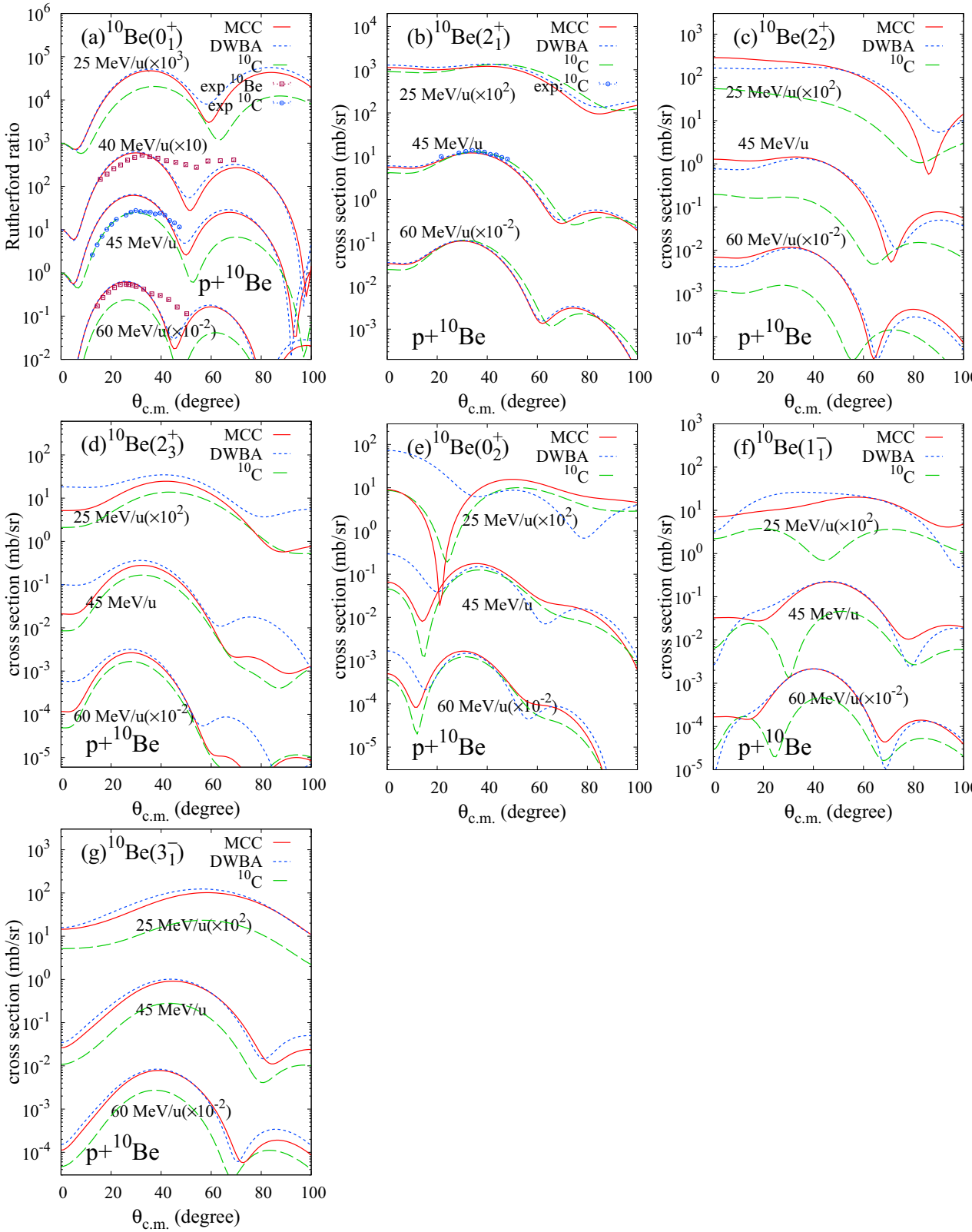

FIG. 11. (a) Elastic and (b)–(g) inelastic cross sections of the ^{10}Be $+p$ and ^{10}C $+p$ reactions for at $E = 25$, 45, 60, and 100 MeV/u. The elastic cross sections of the ^{10}Be $+p$ reaction at $E = 40$ MeV/u are also shown. The MCC and DWBA results of ^{10}Be $+p$ are shown by red solid and blue dashed lines, respectively. The MCC results of ^{10}C $+p$ are shown by green long-dashed lines. The experimental ^{10}Be $+p$ elastic cross sections at $E = 39.1$ MeV/u [64] and $E = 59.4$ MeV/u [63] are shown by red squares in (a). The experimental ^{10}C $+p$ cross sections at $E = 45$ MeV/u [60,65] observed for the 0^+_1 and 2^+_1 states are shown by blue circles in (a) and (b).

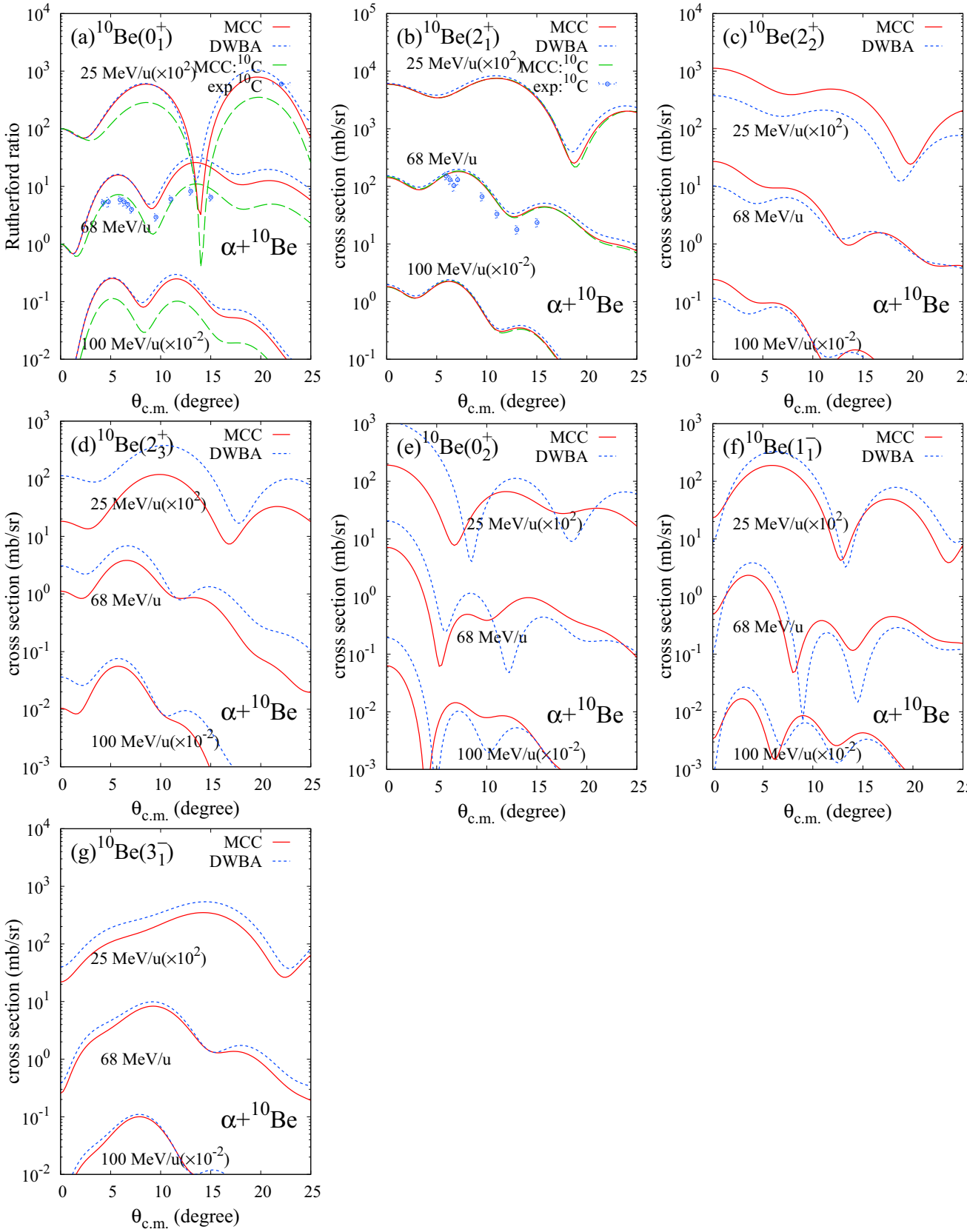

FIG. 12. Calculated (a) elastic and (b)–(g) inelastic cross sections of ^{10}Be $+\alpha$ at $E = 25$, 68, and 100 MeV/u. The MCC and DWBA cross sections are shown by red solid and blue dashed lines, respectively. In (a) and (b), the calculated cross sections of ^{10}C $+\alpha$ are shown by green dashed lines compared with the experimental cross sections at $E = 68$ MeV/u from Ref. [28].

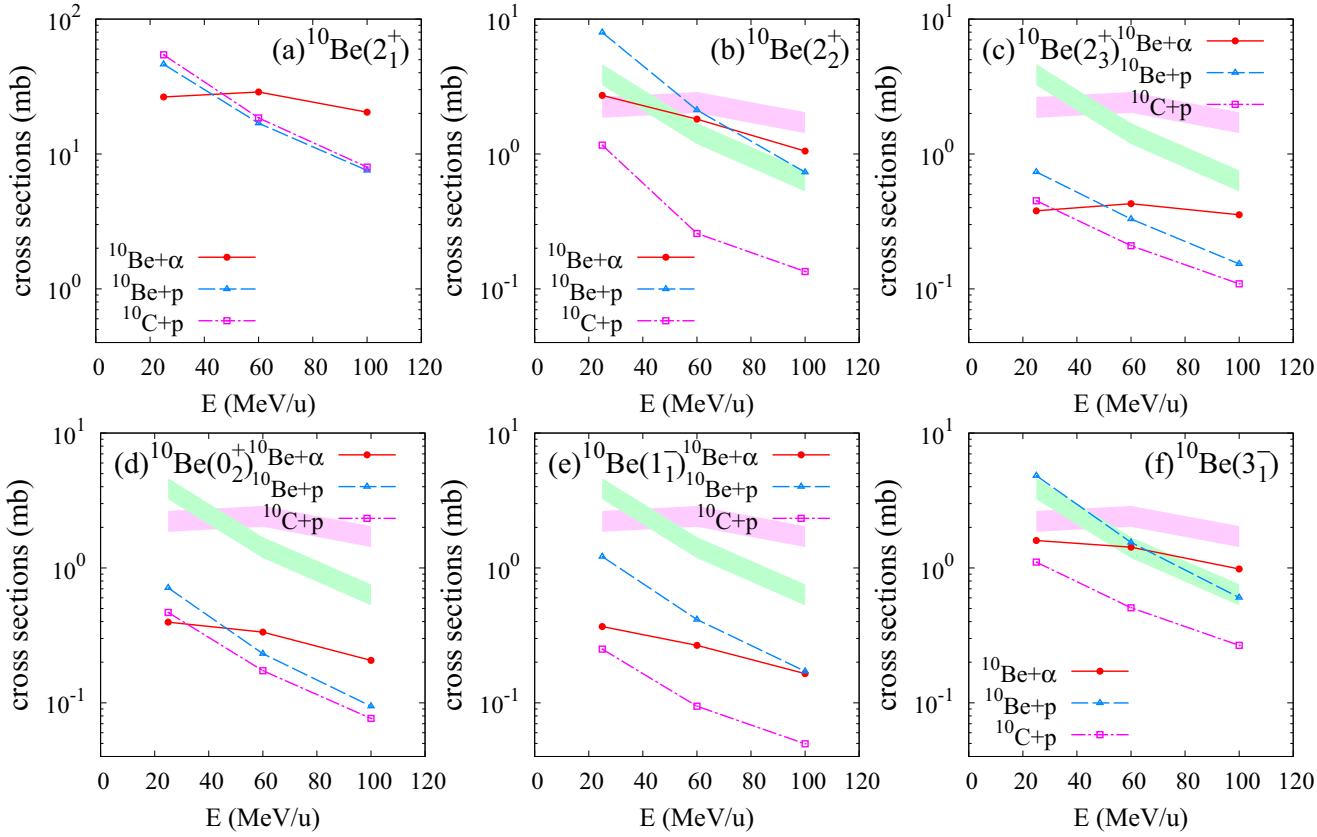

FIG. 13. Integrated cross sections to (a) the 2^+_1 state and (b)–(f) other excited states of ^{10}Be $+p$, ^{10}C $+p$, and ^{10}Be $+\alpha$ inelastic processes are shown by (blue) triangles, (magenta) squares, and (red) circles, respectively. The cross sections at $E = 25$, 60, and 100 MeV/u are calculated with MCC. In panels for the (b) 2^+_2, (c) 2^+_3, (d) 0^+_2, (e) 1^-_1, and (f) 3^-_1 states, 7%–10% of the 2^+_1 cross sections of the ^{10}Be $+p$ and ^{10}Be $+\alpha$ reactions are shown by light-green and pink shaded areas, respectively, as references.

experimental excitation energies of ^{10}Be are used. For the $2^+_1 \to 0^+_1$ transition, the renormalized transition densities are used as explained previously. One-step (DWBA) cross sections are also calculated for comparison. We also calculate the ^{10}C $+p$ and ^{10}C $+\alpha$ reactions assuming the mirror symmetry of diagonal and transition densities between the proton and neutron parts in the $A = 10$ systems. Coulomb shifts of excitation energies are omitted.

In Fig. 10, we show radial dependences and volume integrals of the real and imaginary parts of the present microscopic potential for $p + ^{10}$Be elastic scattering compared with a phenomenological potential of the global optical potential for p elastic scattering [57,58]. The real part of the present $p + ^{10}$Be potential, which are obtained by the g-matrix folding approach with the AMD density, shows a slightly broader radial dependence than the phenomenological potential. This trend is consistent with the expectation from the overestimation of the rms proton radius of ^{10}Be in the present structure calculation.

Figure 11 shows the calculated cross sections of ^{10}Be $+p$ at $E = 25$, 45, and 60 MeV/u together with those of ^{10}C $+p$, and Fig. 12 shows the results of ^{10}Be $+\alpha$ at $E = 25$, 68, and 100 MeV/u. In Figs. 11(a) and 11(b), the results are compared with the experimental ^{10}Be $+p$ data of the elastic cross sections at $E = 39.1$ MeV/u [64] and $E = 59.4$ MeV/u [63] and the ^{10}C $+p$ data of the elastic and 2^+_1 cross sections at $E = 45$ MeV/u [65], which have been observed by the inverse kinematics experiments. The MCC calculations reasonably reproduce those data. It should be noted again that the dip structure of elastic scattering can be smeared by the spin-orbit interaction omitted in the present calculation. As mentioned previously, the present structure calculation overestimates the rms proton radius of the ground state of ^{10}Be. This overestimation may somewhat shift peak and dip positions of the elastic cross sections to forward angles, but the observed data are not enough to discuss details of structure properties, i.e., the proton and neutron density distributions. In Figs. 12(a) and 12(b), we also show the result of the ^{10}C $+\alpha$ reaction compared with the ^{10}C $+\alpha$ data at $E = 68$ MeV/u, which have been recently measured by the inverse kinematics experiment [28]. The observed data of the elastic and 2^+_1 cross sections tend to be smaller than the present result. Comparing the MCC and DWBA results, one can see that CC effects are not minor except for the 2^+_1 and 3^-_1 cross sections of ^{10}Be $+p$ and the 2^+_1 cross sections of ^{10}Be $+\alpha$. At low incident energies, remarkable CC effects can be seen in the 0^+_2 cross sections of ^{10}Be $+p$ and the 2^+_2, 2^+_3, and 0^+_2 cross sections of ^{10}Be $+\alpha$. The CC effects enhance the 2^+_2 cross sections and suppress the 0^+_2 and 2^+_3 cross sections. At higher incident energies, the CC effects become weaker but they remain to

be significant at forward angles even at $E = 60$ MeV/u of ^{10}Be $+p$ and $E = 100$ MeV/u of ^{10}Be $+\alpha$.

Let us compare ^{10}Be $+p$ and ^{10}C $+p$ cross sections. If a transition has the isoscalar character, the difference between ^{10}Be $+p$ and ^{10}C $+p$ cross sections should be small. On the other hand, in the neutron dominant case, it is naively expected that ^{10}Be $+p$ cross sections are enhanced and ^{10}C $+p$ cross sections are relatively suppressed because the p scattering sensitively probes the neutron component rather than the proton component. In Fig. 11, the ^{10}C $+p$ cross sections (green dashed lines) are compared with the ^{10}Be $+p$ cross sections (red solid lines). As expected, the difference is small in the 2^+_1 cross sections, because of the isoscalar nature of the ground-band transition. On the other hand, for the 2^+_2, 1^-_1, and 3^-_1 states, the ^{10}C $+p$ cross sections are remarkably suppressed compared with the ^{10}Be $+p$ cross sections because of the neutron dominant characters of these transitions in ^{10}Be (the proton dominance in ^{10}C).

For quantitative discussions, we compare the integrated cross sections of the inelastic scattering of the ^{10}Be $+p$, ^{10}C $+p$ and ^{10}Be $+\alpha$ reactions. Figure 13 shows the MCC results of the cross sections at $E = 25$, 60, and 100 MeV/u. For the 2^+_1 cross sections, one can see only a small difference between ^{10}Be $+p$ and ^{10}C $+p$. This is a typical example of the isoscalar excitation and can be regarded as reference data to be compared with other excitations. For the side-band 2^+_2 state, the difference between ^{10}Be $+p$ and ^{10}C $+p$ is huge as one order of the magnitude of the cross sections because of the cancellation between proton and neutron components in the ^{10}C $+p$ reaction. As shown in the transition densities [Fig. 9(a)] and the matrix elements (Table III) of ^{10}Be, the proton component of the 2^+_2 transition in ^{10}Be is weak but opposite sign to the neutron one, and it gives the strong cancellation in the mirror transitions probed by the ^{10}C $+p$ reaction. It also gives some cancellation in the isoscalar component probed by the ^{10}Be $+\alpha$ reaction, but the cancellation is tiny in the ^{10}Be $+p$ reaction. The difference of the production rates between the ^{10}Be $+p$ and ^{10}C $+p$ reactions is also large in the 3^-_1 cross section as expected from its remarkable neutron dominance (the ratio $M_n/M_p = 6.4$). Namely, the 3^-_1 cross sections in the ^{10}Be $+p$ reaction are largely enhanced compared to the ^{10}C $+p$ reaction. Similarly, the enhancement of the ^{10}Be $+p$ cross sections is also obtained for the 0^+_2 and 2^+_3 states in the $K^\pi = 0^+_2$ cluster band, but it is not so remarkable as the 3^-_1 state ($M_n/M_p = 6.4$) because of their weaker neutron dominance ($M_n/M_p = 1.89$ of $0^+_1 \to 0^+_2$ and $M_n/M_p = 2.5$ of $0^+_1 \to 2^+_3$). It is rather striking that, the difference in the 1^-_1 production rates between ^{10}Be $+p$ and ^{10}C $+p$ is unexpectedly large even though the neutron dominance of the 1^-_1 state is weaker as $M_n/M_p = 1.46$ than the 2^+_3 and 0^+_2 states. This is understood by the difference in radial behaviors of the proton and neutron transition densities. As shown in Fig. 9(c) for the $0^+_1 \to 1^-_1$ transition densities, the neutron amplitude is dominant in the outer region and enhances the ^{10}Be $+p$ cross sections. Moreover, at the surface region of $r = 2$-3 fm, the proton transition density is opposite to the neutron one and gives the cancellation effect in the ^{10}C $+p$ reaction.

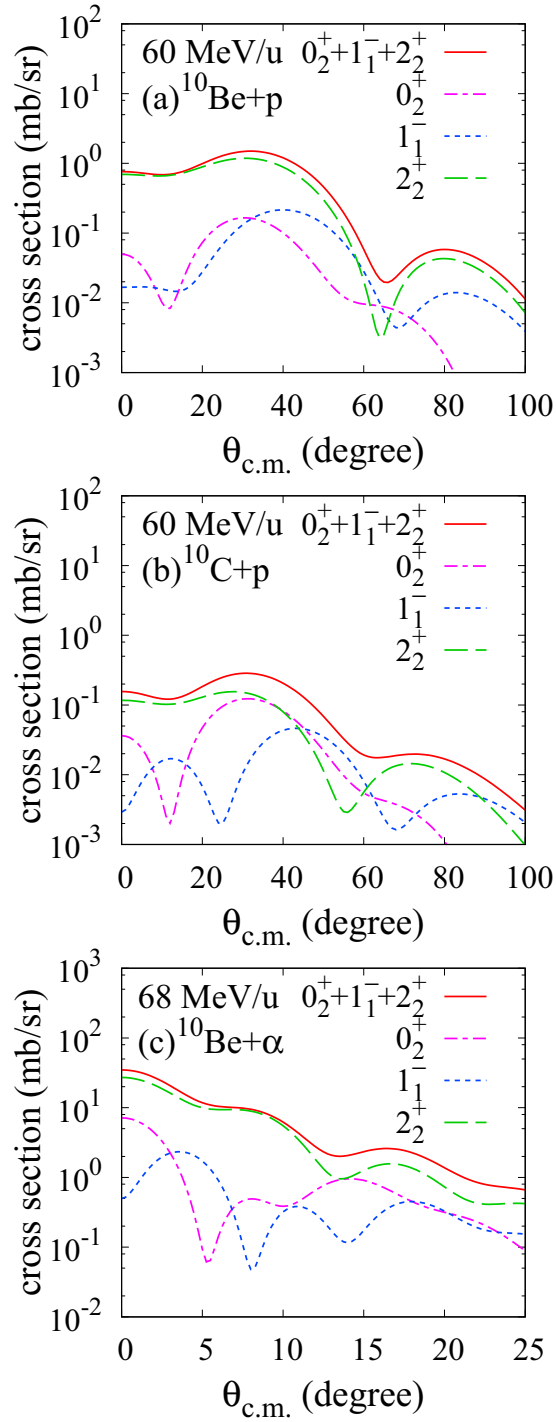

FIG. 14. The 0^+_2, 1^-_1, and 2^+_2 cross sections of the ^{10}Be $+p$, ^{10}C $+p$, and ^{10}Be $+\alpha$ reactions obtained by the MCC calculations. (a)^{10}Be $+p$ at $E = 60$ MeV/u, (b)^{10}C $+p$ at $E = 60$ MeV/u, and (c)^{10}Be $+\alpha$ at $E = 68$ MeV/u. The 0^+_2, 1^-_1, and 2^+_2 cross sections and their incoherent sum are shown by magenta dot-dashed, blue dashed, green long-dashed, and red solid lines.

In the experimental side, the (p, p') and (α, α') cross sections off ^{10}Be and ^{10}C have been measured only for the 2^+_1 state. Indeed, according to the present calculation, the 2^+_1 state is strongly populated in p and α inelastic scattering processes,

but other states are relatively weak as more than one order smaller cross sections than the 2_1^+ state. Below, we discuss sensitivity of the ^{10}Be $+p$, ^{10}Be $+\alpha$, and ^{10}C $+p$ reactions to observe higher excited states above the 2_1^+ state.

First, we examine the integrated cross sections and discuss the production rates of excited states and their projectile and energy dependencies. In Figs. 13(b)–13(f), 7%–10% of the 2_1^+ cross sections of the ^{10}Be $+p$ and ^{10}Be $+\alpha$ reactions are shown by light-green and pink shaded areas, respectively. We consider these areas as references of one-order smaller magnitude of the 2_1^+ cross sections for comparison. For the side-band 2_2^+ transition [Fig. 13(b)], the ^{10}Be $+p$ cross sections (blue dashed line) exceed the 7%–10% area (light-green) indicating that the ^{10}Be $+p$ reaction can be an efficient tool to observe the neutron dominance of the 2_2^+ excitation. Also the ^{10}Be $+\alpha$ cross sections (red solid lines) reach 10% of the 2_1^+ cross sections at $E = 25$ MeV/u but decrease at high energies. For the 3_1^- transitions [Fig. 13(f)], the ^{10}Be $+p$ cross sections (blue dashed line) are within the 7%–10% area (light-green), and the ^{10}Be $+\alpha$ cross sections are approximately 5% of the 2_1^+ cross sections. For other states, the population is much weaker as 1%–2% of the 2_1^+ state or less.

Next, we compare the 0_2^+, 2_2^+, and 1_1^- cross sections of each reaction. Since these three states almost degenerate around $E_x \approx 6$ MeV in the experimental energy spectra, it may be difficult to resolve observed cross sections to individual states. In Figs. 14(a), 14(b) and 14(c), the calculated cross sections of ^{10}Be $+p$ at $E = 60$ MeV/u, ^{10}C $+p$ at $E = 60$ MeV/u, and ^{10}Be $+\alpha$ at $E = 68$ MeV/u are shown, respectively. The cross sections of each state and the incoherent sum of three states are plotted. In the ^{10}Be $+p$ reaction, the 2_2^+ cross sections dominate the summed cross sections while the 0_2^+ and 1_1^- contributions are minor. In the ^{10}C $+p$ reaction, where the 2_2^+ cross sections are strongly suppressed, the magnitude of the 0_2^+ cross sections is comparable to that of 2_2^+ in the $\theta_{\rm c.m.} = 20$-40° range, and the 1_1^- state gives major contribution at $\theta_{\rm c.m.} \approx 50^\circ$ and smears the second dip of the 2_2^+ cross sections in the summed cross sections. In the ^{10}Be $+\alpha$ reaction at forward angles, the 0_2^+ and 1_1^- contributions are minor compared to the dominant 2_2^+ contribution. It seems to contradict the usual expectation that forward angle α scattering can be generally useful to observe monopole transitions. But it is not the case in the ^{10}Be $+\alpha$ reaction because the 0_2^+ cross sections at forward angles are strongly suppressed by the CC effect. Alternatively, detailed analysis of ^{10}C $+p$ cross sections in a wide range of scattering angles may be promising to observe the 0_2^+ and 1_1^- states.

It should be commented that the predicted cross sections still contain structure model ambiguity, in particular, for the cluster bands. Basis configurations adopted in the present AMD calculation are not enough to describe details of the intercluster motion, which may somewhat enhance the monopole transition strengths.

V. SUMMARY

Isospin characters of nuclear excitations in ^{26}Mg and ^{10}Be were investigated with the MCC calculations of p and α inelastic scattering. The structure calculations of ^{26}Mg and ^{10}Be were done by antisymmetrized molecular dynamics (AMD). In the AMD calculations, the $K^\pi = 0^+$ ground and $K^\pi = 2^+$ side bands were obtained in ^{26}Mg and ^{10}Be. In both systems, the ground-band $2_1^+(K^\pi = 0_1^+)$ state and the side-band $2_2^+(K^\pi = 2^+)$ state have quite different isospin characters. The former has the isoscalar feature and the latter shows the neutron dominance character. This can be a general feature in $N = Z + 2$ system having a prolately deformed $N = Z$ core surrounded by valence neutrons.

The MCC calculations of p and α inelastic scattering off ^{26}Mg and ^{10}Be were performed with the Melbourne g-matrix folding approach by using the matter and transition densities of the target nuclei calculated with AMD. The calculations reasonably reproduced the observed 0_1^+, 2_1^+, and 2_2^+ cross sections of ^{26}Mg $+p$ scattering at $E_p = 24$ and 40 MeV and of ^{26}Mg $+\alpha$ scattering at $E_\alpha = 104$ and 120 MeV. It was shown that the ^{26}Mg $+p$ scattering is a sensitive probe to the neutron component of the $0_1^+ \to 2_2^+$ transition. In the present analysis, the neutron transition matrix element $M_n \approx 8$ fm^2 (the squared ratio $|M_n/M_p|^2 \approx 7$) of the $0_1^+ \to 2_2^+$ transitions in ^{26}Mg is favored to reproduce the ^{26}Mg $+p$ and ^{26}Mg $+\alpha$ cross sections consistently.

For ^{10}Be $+p$ and ^{10}Be $+\alpha$ scattering, inelastic cross sections to the excited states in the $K^\pi = 0_1^+$ ground, $K^\pi = 2^+$ side, $K^\pi = 0_2^+$ cluster, and $K^\pi = 1^-$ cluster bands were discussed. In a comparison of the ^{10}Be $+p$, ^{10}C $+p$, and ^{10}Be $+\alpha$ reactions, the isospin characters of transitions in inelastic scattering processes were investigated. Also in ^{10}Be, the p inelastic scattering was found to be a sensitive probe to the neutron dominance in the 2_2^+ excitation. The significant suppression of the 2_2^+ cross sections of ^{10}C $+p$ was obtained because of the cancellation of the proton and neutron components in the transition. The present prediction of the inelastic scattering off ^{10}Be may be useful for the feasibility test of future experiments in the inverse kinematics.

ACKNOWLEDGMENTS

The authors thank Dr. Furuno and Dr. Kawabata for fruitful discussions. The computational calculations of this work were performed by using the supercomputer in the Yukawa Institute for theoretical physics, Kyoto University. This work was partly supported by Grants-in-Aid of the Japan Society for the Promotion of Science (Grants No. JP18K03617, No. JP16K05352, and No. 18H05407) and by the grant for the RCNP joint research project.

[1] A. M. Bernstein, V. R. Brown, and V. A. Madsen, Phys. Lett. B **71**, 48 (1977).

[2] A. M. Bernstein, V. R. Brown, and V. A. Madsen, Phys. Rev. Lett. **42**, 425 (1979).

[3] A. M. Bernstein, V. R. Brown, and V. A. Madsen, Phys. Lett. B **103**, 255 (1981).
[4] B. A. Brown and B. H. Wildenthal, Phys. Rev. C **21**, 2107 (1980).
[5] B. A. Brown *et al.*, Phys. Rev. C **26**, 2247 (1982).
[6] C. L. Morris, S. J. Seestrom-Morris, D. Dehnhard, C. L. Blilie, R. Gilman, G. P. Gilfoyle, J. D. Zumbro, M. G. Burlein, S. Mordechai, H. T. Fortune, L. C. Bland, M. Brown, D. P. Saunders, P. A. Seidl, C. F. Moore, K. Maeda, G. S. Blanpied, and B. A. Brown, Phys. Rev. C **35**, 1388 (1987).
[7] S. Iversen *et al.*, Phys. Rev. Lett. **40**, 17 (1978).
[8] P. Grabmayr, J. Rapaport, and R. W. Finlay, Nucl. Phys. A **350**, 167 (1980).
[9] J. Kelly *et al.*, Phys. Lett. B **169**, 157 (1986).
[10] T. K. Alexander, G. C. Ball, W. G. Davies, J. S. Forster, I. V. Mitchell, and H.-B. Mak, Phys. Lett. B **113**, 132 (1982).
[11] C.-A. Wiedner, K. R. Cordell, W. Saathoff, S. T. Thornton, J. Bolger, E. Boschitz, G. Proebstle, and J. Zichy, Phys. Lett. B **97**, 37 (1980).
[12] P. W. F. Alons, H. P. Blok, J. F. A. V. Hienen, and J. Blok, Nucl. Phys. A **367**, 41 (1981).
[13] B. Zwieglinski, G. M. Crawley, J. A. Nolen, and R. M. Ronningen, Phys. Rev. C **28**, 542 (1983).
[14] K. Van Der Borg, M. N. Harakeh, and A. Van Der Woude, Nucl. Phys. A **365**, 243 (1981).
[15] Y. Kanada-En'yo and H. Horiuchi, Phys. Rev. C **55**, 2860 (1997).
[16] H. Iwasaki *et al.*, Phys. Lett. B **481**, 7 (2000).
[17] Y. Kanada-En'yo, Phys. Rev. C **71**, 014310 (2005).
[18] Y. Kanada-En'yo, Phys. Rev. C **71**, 014303 (2005).
[19] H. Sagawa, X. R. Zhou, X. Z. Zhang, and T. Suzuki, Phys. Rev. C **70**, 054316 (2004).
[20] M. Takashina, Y. Kanada-En'yo, and Y. Sakuragi, Phys. Rev. C **71**, 054602 (2005).
[21] H. J. Ong *et al.*, Phys. Rev. C **73**, 024610 (2006).
[22] T. J. Bürvenich, W. Greiner, L. Guo, P. Klüpfel, and P. G. Reinhard, J. Phys. G **35**, 025103 (2008).
[23] M. Takashina and Y. Kanada-En'yo, Phys. Rev. C **77**, 014604 (2008).
[24] Z. Elekes, N. Aoi, Zs. Dombrádi, Zs. Fülöp, T. Motobayashi, and H. Sakurai, Phys. Rev. C **78**, 027301 (2008).
[25] M. Wiedeking *et al.*, Phys. Rev. Lett. **100**, 152501 (2008).
[26] J. M. Yao, J. Meng, P. Ring, Z. X. Li, Z. P. Li, and K. Hagino, Phys. Rev. C **84**, 024306 (2011).
[27] C. Forssén, R. Roth, and P. Navrátil, J. Phys. G **40**, 055105 (2013).
[28] T. Furuno *et al.*, Phys. Rev. C **100**, 054322 (2019).
[29] W. von Oertzen, M. Freer, and Y. Kanada-En'yo, Phys. Rep. **432**, 43 (2006).
[30] Y. Kanada-En'yo, M. Kimura, and A. Ono, Prog. Theor. Exp. Phys. **2012**, 01A202 (2012).
[31] M. Ito and K. Ikeda, Rep. Prog. Phys. **77**, 096301 (2014).
[32] Y. Kanada-En'yo, Phys. Rev. C **84**, 024317 (2011).
[33] K. Amos, P. J. Dortmans, H. V. von Geramb, S. Karataglidis, and J. Raynal, in *Advances in Nuclear Physics*, Vol. 25, edited by J. W. Negele and E. Vogt (Plenum, New York, 2000), p. 275.
[34] S. Karataglidis, Y. J. Kim, and K. Amos, Nucl. Phys. A **793**, 40 (2007).
[35] K. Minomo, K. Ogata, M. Kohno, Y. R. Shimizu, and M. Yahiro, J. Phys. G **37**, 085011 (2010).
[36] M. Toyokawa, K. Minomo, and M. Yahiro, Phys. Rev. C **88**, 054602 (2013).
[37] K. Minomo, K. Washiyama, and K. Ogata, arXiv:1712.10121.
[38] K. Egashira, K. Minomo, M. Toyokawa, T. Matsumoto, and M. Yahiro, Phys. Rev. C **89**, 064611 (2014).
[39] K. Minomo and K. Ogata, Phys. Rev. C **93**, 051601(R) (2016).
[40] Y. Kanada-En'yo and K. Ogata, Phys. Rev. C **99**, 064601 (2019).
[41] Y. Kanada-En'yo and K. Ogata, Phys. Rev. C **99**, 064608 (2019).
[42] Y. Kanada-En'yo and K. Ogata, Phys. Rev. C **100**, 064616 (2019).
[43] Y. Kanada-En'yo and K. Ogata, Phys. Rev. C **101**, 064607 (2020).
[44] Y. Kanada-En'yo, H. Horiuchi, and A. Ono, Phys. Rev. C **52**, 628 (1995).
[45] Y. Kanada-En'yo, Phys. Rev. Lett. **81**, 5291 (1998).
[46] Y. Kanada-En'yo, H. Horiuchi, and A. Dote, Phys. Rev. C **60**, 064304 (1999).
[47] T. Ando, K. Ikeda, and A. Tohsaki, Prog. Theor. Phys. **64**, 1608 (1980).
[48] R. Tamagaki, Prog. Theor. Phys. **39**, 91 (1968).
[49] N. Yamaguchi, T. Kasahara, S. Nagata, and Y. Akaishi, Prog. Theor. Phys. **62**, 1018 (1979).
[50] A. Nagel *et al.*, J. Phys. A **7**, 1697 (1974).
[51] J. L. Durell *et al.*, J. Phys. A **5**, 302 (1972).
[52] M. S. Basunia and A. M. Hurst, Nucl. Data Sheets **134**, 1 (2016).
[53] D. R. Tilley, J. H. Kelley, J. L. Godwin, D. J. Millener, J. E. Purcell, C. G. Sheu, and H. R. Weller, Nucl. Phys. A **745**, 155 (2004).
[54] I. Angeli and K. P. Marinova, At. Data Nucl. Data Tables **99**, 69 (2013).
[55] E. W. Lees, A. Johnston, S. W. Brain, C. S. Currant, W. A. Gillespie, and R. P. Singhal, J. Phys. A **7**, 936 (1974).
[56] R. Soundranayagam, A. Saha, K. K. Seth, C. de Jager, H. de Vries, H. Blok, and G. van der Steenhoven, Phys. Lett. B **212**, 13 (1988).
[57] S. Hama, B. C. Clark, E. D. Cooper, H. S. Sherif, and R. L. Mercer, Phys. Rev. C **41**, 2737 (1990).
[58] E. D. Cooper, S. Hama, B. C. Clark, and R. L. Mercer, Phys. Rev. C **47**, 297 (1993).
[59] V. Avrigeanu, P. E. Hodgson, and M. Avrigeanu, Phys. Rev. C **49**, 2136 (1994).
[60] N. Otuka *et al.*, Nucl. Data Sheets **120**, 272 (2014).
[61] B. A. Brown, A. Arima, and J. B. McGrory, Nucl. Phys. A **277**, 77 (1977).
[62] H. Rebel, G. W. Schweimer, G. Schatz, J. Specht, R. Löhken, G. Hauser, D. Habs, and H. Klewe-Nebenius, Nucl. Phys. A **182**, 145 (1972).
[63] M. D. Cortina-Gil *et al.*, Phys. Lett. B **401**, 9 (1997).
[64] V. Lapoux, N. Alamanos, F. Auger, Y. Blumenfeld, J. Casandjian, M. Chartier, M. Cortina-Gil, V. Fekou-Youmbi, A. Gillibert, M. Mac Cormick, F. Marechal, F. Marie, W. Mittig, F. Santos de Oliveira, N. Orr, A. Ostrowski, S. Ottini-Hustache, P. Roussel-Chomaz, J. Scarpaci, J. Sida, T. Suomijarvi, and J. Winfield, Phys. Lett. B **658**, 198 (2008).
[65] C. Jouanne *et al.*, Phys. Rev. C **72**, 014308 (2005).